1   **Distributed normal faulting in the tip zone of the South Alkyonides Fault System,**

2   **Gulf of Corinth, constrained using ^{36}Cl exposure dating of Late-Quaternary wave-cut**

3   **platforms.**

4

5   J. Robertson[a*], G.P. Roberts[a], F. Iezzi[a], M. Meschis[a], D. M. Gheorghiu[b], D. Sahy[c], C. Bristow[d], C.

6   Sgambato[e]

7   [a]Department of Earth and Planetary Sciences, Birkbeck College, University of London, WC1E

8   7HX, UK.

9   [b] Scottish Universities Environmental Research Centre, Scottish Enterprise Technology Park,

10   Rankine Avenue, Glasgow, G75 0QF, UK

11   [c] British Geological Survey, Keyworth, Nottingham, NG12 5GG, UK

12   [d]Arcadis Consulting Ltd, London, UK

13   [e] Institute for Risk and Disaster Reduction, University College London, Gower Street, Kings

14   Cross, London, WC1E 6BS UK

15

16   Corresponding author: Jenni Robertson (j.robertson@praxisuk.co.uk)

17

18   Abstract

19

20   The geometry, rates and kinematics of active faulting in the region close to the tip of a major

21   crustal-scale normal fault in the Gulf of Corinth, Greece, are investigated using detailed fault

22   mapping and new absolute dating. Fault offsets have been dated using a combination of

23   ^{234}U/^{230}Th coral dates and *in situ* ^{36}Cl cosmogenic exposure ages for sediments and wave-cut

24   platforms deformed by the faults. Our results show that deformation in the tip zone is

25   distributed across as many as eight faults arranged within ~700 m across strike, each of which

26   deforms deposits and landforms associated with the 125 ka marine terrace of Marine Isotope

27   Stage 5e. Summed throw-rates across strike achieve values as high as 0.3-1.6 mm/yr, values

28   that are comparable to those at the centre of the crustal-scale fault (2-3 mm/yr from

29   Holocene palaeoseismology and 3-4 mm/yr from GPS geodesy). The relatively high

30   deformation rate and distributed deformation in the tip zone are discussed in terms of stress

31   enhancement from rupture of neighbouring crustal-scale faults and in terms of how this

32   should be considered during fault-based seismic hazard assessment.

33

34

35   1. **Introduction**

36   Understanding the deformation that occurs at the tips of normal faults is important

37   because (a) it contributes to knowledge on fault growth and linkage (e.g. Cowie and Shipton,

38   1998; Peacock and Sanderson, 1991; McLeod et al., 2000; Peacock, 2002), (b) has the

39   potential to inform fault-based seismic hazard analysis about fault connectivity and maximum

40   rupture extent (Scholz and Gupta, 2000), and (c) influences our understanding of fluid

41   connectivity or otherwise of faulted hydrocarbon reservoirs (Yielding et al., 1996). One of the

42   key observations from studies on tip-zone deformation is that the shape of the displacement

43   gradients differs between isolated and interacting faults as a result of perturbation to the

44   surrounding stress field (Peacock and Sanderson, 1991; Willemse et al., 1996; Cartright and

45   Mansfield, 1998; Cowie and Shipton, 1998; Scholz and Lawler, 2004). In particular, steeper

46   displacement gradients occur close to fault tips where adjacent faults are in close proximity

47   (Gupta and Scholz, 2000). However, it is not known how these steep displacement gradients

48   develop through time, whether displacement is always localised on a single fault or spread

49   across several fault strands, and how tip deformation should be incorporated into studies of

50   seismic hazard. To address these questions, this paper provides measurements of

51   deformation rates across all faults within a tip zone over timescales that allow one to

52   recognise how many individual faults are active simultaneously.

53   Our interest was raised for this topic because we note that at the tips of some crustal-

54   scale faults, distributed faulting dominates as networks of splay faults that form at acute

55   angles to the main fault (McGrath and Davison, 1995; Perrin et al., 2016) (Figure 1). It is

56   unclear whether these fault patterns and the resultant deformation can be more complex

57   where the tips of two crustal-scale faults overlap along strike and interaction occurs between

58   neighbouring faults (Gupta and Scholz, 2000). Moreover, although typically fault

59   displacement decreases to minimal values toward the tip (Cowie and Roberts, 2001), a shared

60   tip zone can host high displacement gradients relative to the main fault (Peacock and

61   Sanderson, 1991; 1994; Schlische et al., 1996) and it is unclear if this is accommodated by

62   deformation spread across multiple faults or localised on a single fault.

63   A detailed analysis of the deformation within a fault tip zone has the capacity to

64   contribute to fault-based seismic hazard assessment (e.g. Pace et al., 2016). If tip zones

65   contain relatively-high displacements, distributed across multiple faults, or localised on a

66   single fault, this may influence whether ruptures can cross the tip zone onto other

67   neighbouring faults (e.g. Field et al. 2014), influencing estimates of maximum earthquake

68   magnitude (Wells and Coppersmith, 1994). However, the lack of measured displacement data

69   within tip zones means that historic fault-based seismic hazard approaches typically rely on

70   throw/slip rate data from outside the tip zone and the assumption that displacement

71   gradients decrease toward the tips according to pre-ordained fault shapes (Faure Walker et

72   al., 2018). The above assumptions produce significant uncertainty in Probabilistic Seismic

73   Hazard Assessment (PSHA) (Pace et al., 2016), and have been shown to result in large

74   differences between calculations of recurrence intervals and ground-shaking exceedance

75   probabilities for different fault geometries (Faure Walker et al., 2018). Constraining the rates

76   of deformation at multiple locations along a fault, including within the tip-zone, is therefore

77   a vital component of reducing the uncertainty in PSHA. Furthermore, this may be particularly

78   important if this analysis is carried out in an area where overlapping tip zones occur; higher

79   displacement gradients, and consequently slip/throw rates, may mean that cumulative slip

80   rates may be relatively high, even when compared to 'on fault' values.

81   One of the main challenges to gaining insights of how tip-zone deformation

82   accumulates through time, over timescales relevant to earthquake rupture, is to derive

83   knowledge of the timescales over which faulting occurs. Existing approaches use

84   measurements of vertical displacement, coupled with the ages of offset strata/landforms (e.g.

85   Sieh et al. 1989; Armijo et al. 1991; Roberts and Michetti, 2004; Galli et al., 2008; Schlagenhauf

86   et al., 2010, Mozafari et al. 2019; Robertson et al., 2019). In tip zones where distributed

87   faulting dominates and slip-rate along individual faults may be (a) relatively low, and (b)

88   difficult to detect, it may be advantageous to concentrate on techniques that average the slip

89   over relatively long time periods. Investigations using deformed Quaternary marine terraces

90   and their associated wave-cut platforms (e.g. Armijo et al., 1996; Roberts et al., 2009, Roberts

91   et al., 2013; Binnie et al., 2016; Jara-Munoz et al., 2017; Meschis et al., 2018; Robertson et al.,

92   2019) allow deformation rates to be measured over $10^{4\text{-}5}$ years, and therefore displacement

93   associated with the very low slip rates of individual tip-zone faults can be resolved.

94   The western tip area of the north dipping South Alkyonides Fault System (SAFS)

95   (Morewood and Roberts, 1997), located on the Perachora Peninsula (eastern Gulf of Corinth,

96   Greece) provides an opportunity to study the throw rate, 'off-fault' deformation and possible

97   interaction with neighbouring faults. A set of distributed faults at Cape Heraion, in the far

98   west of the Perachora Peninsula, represents the western tip zone of the SAFS (Morewood and

99   Roberts, 1997) (Figure 2). While this area has been studied before (Morewood and Roberts,

100 1997), this study lacked the detailed mapping of displacement gradients along individual

101 faults, and the age constraints needed to be able to fully examine the rates and spatial

102 variation of deformation. Morewood and Roberts (1997) identified faulted offsets of what

103 they claim is a single marine terrace. Others have made an alternative interpretation where

104 marine terraces at different elevations are not faulted, but instead date from different sea-

105 level highstands (Leeder et al., 2003; Leeder et al., 2005). This disagreement could not be

106 resolved, because although some age constraints were available from ^{234}U/^{230}Th dating of

107 corals (Vita-Finzi et al., 1993, Leeder et al., 2003; Leeder et al., 2005; Roberts et al., 2009;

108 Houghton, 2010), ages were not available for marine terrace deposits at different elevations.

109   Our breakthrough reported herein, is that our detailed mapping revealed that the

110 coral-bearing strata can be mapped along strike into wave-cut platforms, and wave-cut

111 platforms can be dated using *in situ* ^{36}Cl cosmogenic exposure studies (Robertson et al. 2019).

112 Here we test the hypothesis of Morewood and Roberts (1997) of a single, faulted

113 palaeoshoreline by (i) constraining the ages of marine terrace deposits and landforms at

114 different elevations, (ii) calculating individual and cumulative fault throw values and, (iii)

115 exploring how these vary spatially within the tip zone and how they compare to other normal

116 fault tip zones. The results of these analyses are combined with those from Coulomb stress

117 change modelling to explore the interaction of the tip of the SAFS with neighbouring faults.

118 These findings are then discussed in the context of fault-based probabilistic seismic hazard

119 assessment.

120

2. **Background**

2.1 Tectonic setting

The Perachora Peninsula is located within the eastern Gulf of Corinth (Figure 2), one of the world's fastest extending rift systems, with extension rates between <5 mm/yr and 10-15 mm/yr (Davies et al., 1997; Clarke et al., 1998; Briole et al., 2000). The presence of a complex basin structure (e.g. Moretti et al., 2003; Sachpazi et al., 2003; McNeill et al., 2005; Sakellariou et al., 2007; Bell et al., 2009; Nixon et al., 2016; Gawthorpe et al., 2018) is a consequence of extension accommodated along sets of north and south dipping faults. From the Late Quaternary to the present day, north-dipping faults located along the rift system that borders the south of the gulf are predominately responsible for extension, with other faults less active or ceasing activity (Sakellariou et al., 2007; Bell et al., 2009; Roberts et al., 2009; Nixon et al., 2016; Fernandez-Blanco et al., 2019). The north-dipping faults have been shown to have started to dominate the deformation between 340-175 ka (Roberts et al., 2009; Nixon et al., 2016).

The Perachora Peninsula is located between the Alkyonides Gulf to the north and the Lechaion Gulf to the south (Figure 2a). This area is dominated by two crustal-scale, north-dipping, active fault systems, the East Xylocastro Fault System (EXFS) (so named in this study) and the South Alkyonides Fault System (SAFS) (Figure 2a). The EAFS is formed by the East Xylocastro, North Kiato and Perachora faults, located offshore and arranged en-echelon. The linkage of these three faults is unclear (Bell et al., 2009) with some authors suggesting fault connections at depth (Armijo et al., 2006; Nixon et al., 2016) and others suggesting that they are isolated faults (Stefatos et al., 2002; Moretti et al., 2003; Sakellariou et al., 2007). The presence of a set of coherent terraces in the footwall of the East Xylocastro, North Kiato and

145 Perachora faults (Armijo et al., 2006) combined with the formation of a single depocentre

146 bounding the north-dipping faults on the south side of the gulf (Nixon et al., 2016) has been

147 cited as evidence to support a through-going fault that is connected at depth.

148   The predominantly onshore, ~40 km long SAFS is comprised of the Pisia, Skinos, East

149 Alkyonides and Psatha faults (Figure 2, Roberts, 1996a; Morewood and Roberts, 1997; 1999;

150 2001; 2002; Leeder et al., 2005; Roberts et al., 2009). Analysis of the fault system shows that

151 slip vectors converge toward its centre (Roberts, 1996a; 1996b) where a maximum

152 cumulative throw of 2500 m is recorded (Morewood and Roberts, 2002), which decreases

153 toward both tips (Roberts, 1996a; Morewood and Roberts, 1999; Roberts et al., 2009). In the

154 western section of the SAFS, decreasing offset is reflected in deformed Late Quaternary

155 palaeoshorelines and Holocene notches in the footwall (Cooper et al., 2007; Roberts et al.,

156 2009), where uplift rates decrease from 0.52 mm/yr to 0.25 mm/yr from east to west in the

157 most western 5 km of the fault. Roberts et al. (2009) identified that the SAFS experienced an

158 increase in slip rate since ~175 ka by a factor of ~3, suggested to be linked to the cessation of

159 faulting on neighbouring across-strike faults.

160   Evidence from recent earthquakes combined with Holocene throw and slip rate data

161 provide insight into the activity of faults within the SAFS over decadal to 10^3 year timescales.

162 Specifically, analysis of post-LGM slip on the Pisia fault revealed maximum slip rates of 2.3

163 mm/yr during the Holocene (Mechernich et al., 2018). Palaeoseismic trenching along the

164 Skinos fault yielded throw rates of 1.2-2.5 mm/yr over ~1500 years (Collier et al., 1998). Two

165 >Ms 6 earthquakes on the 24th and 25th February 1981 are reported to have partially ruptured

166 faults within the SAFS (Jackson et al., 1982; Roberts, 1996a; Collier et al., 1998). Ruptures in

167 bedrock and alluvium that extend for 15-20 km (Jackson et al., 1982; Bornovas et al., 1984;

168 Roberts, 1996a) were observed following the February 1981 earthquakes, with maximum

169   coseismic throw values of 150 cm and 100 cm identified on the Pisia and Skinos faults

170   respectively (Jackson et al., 1982).

171   The February 1981 earthquake ruptures were mapped to a throw minima along the

172   south of Lake Vouliagmeni (Figure 2c) (Bornovas, 1984; Roberts, 1996a; Morewood and

173   Roberts, 1999) where the "throw and geomorphic expression across [the SAFS] tend to zero"

174   (Morewood and Roberts, 1999) and were used to conclude that the SAFS does not extend

175   beyond the western end of the lake. Consequently, this location was identified as the western

176   fault tip of the SAFS (Morewood and Roberts, 1999, Figure 4a) ('A' on Figure 2c). The area to

177   the west of this location, Cape Heraion, is deformed by numerous normal faults, providing an

178   excellent opportunity to explore deformation close to the tip of a normal fault.

179

180   2.2 *Cape Heraion, Perachora Peninsula*

181   The extreme west of the Perachora Peninsula, Cape Heraion, is located beyond the

182   western tip of the SAFS (as defined by Morewood and Roberts, 1999, Figure 2c). It is bounded

183   to the north by the Perachora fault segment, the most eastern fault within the EXFS, and to

184   the south by the south dipping, active Heraion fault (Taylor et al., 2011; Charalampakis et al.,

185   2014; Nixon et al., 2016) (Figure 2a). The geology of Cape Heraion is comprised of a succession

186   of deposits from the Mesozoic to the Late Quaternary with more recent Late Quaternary-

187   Holocene geomorphic features imprinted such as wave-cut platforms and Holocene sea-level

188   notches.

189   The stratigraphic succession of the Cape comprises Mesozoic basement limestones

190   unconformably overlain by Plio-Pleistocene marls and sandstones that are, in turn, overlain

191   by algal mound bioherms (also known as cyanobacterial mounds) above which a bioclastic

192   shallow-marine coral-bearing sediment occurs (Bornovas, 1984; see Portman et al., 2005 for

descriptions of each lithology). The bioherms are dominated by freshwater branched

cyanobacterium *Rivularia haematites*, suggested to have formed when the Gulf of Corinth

was a lake (Kershaw and Guo, 2001, 2003, 2006). Domal-topped bioherms in the hangingwall

and flat-topped bioherms in the footwall suggest they grew up to water level during faulting

with restricted vertical growth in the footwall (Kewshaw and Guo, 2006). Subsequent relative

sea-level rise resulted in the presence of a marine bioclastic layer above the bioherms

(Portman et al., 2005; Roberts et al., 2009) and caves containing marine biota within the

bioherms (Kershaw and Guo, 2006). Taken together, the above evidence is suggestive that

faults were active during initial freshwater conditions, that were subsequently changed to

marine by a relative sea-level rise. However, these lines of evidence are debated by other

authors (Leeder et al., 2005; Portman et al., 2005; Andrews et al., 2007), who favour that the

bioherms grew in a marine environment.

The observed geomorphology on Cape Heraion resembles that of a 'stepped' profile

with horizontal surfaces (terraces) separated by steep slopes. The sub-horizontal surfaces are

interpreted as marine terraces because they are associated with coralliferous sediments,

marine shoreface deposits with Quaternary marine fossils, and wave-cut platforms that are

commonly bored by marine lithophagid borings (Morewood and Roberts, 1997, 1999; Leeder

et al., 2003; Leeder et al., 2005; Roberts et al., 2009). Quaternary marine terraces typically

form during glacio-eustatic sea-level highstands that occur as a response to glacial melting

during interglacial periods. At the up-dip terminations of the marine terraces, it is common to

find wave-cut notches and platforms that host features such as lithophagid borings and inter-

tidal millholes, indicative of formation at palaeoshorelines (Westaway 1993; Griggs et al.,

1994; Miller and Mason, 1994; Roberts et al., 2009; Robertson et al., 2019).

216   Although the marine terraces and intertidal palaeoshoreline indicators are widely

217   accepted, the explanation for the steep slopes separating marine terraces is debated on Cape

218   Heraion. The slopes are interpreted in two ways by different authors: (1) as palaeo- sea-cliffs,

219   cut by wave-action by three successive Quaternary glacioeustatic sea-level highstands

220   (Leeder et al., 2003; Leeder et al., 2005) (Figure 3a); (2) the locations of faults offsetting a

221   single terrace surface, where the up-dip termination of a terrace surface at a slope is the

222   hangingwall cut-off of the marine terrace along the fault (Figure 3b; Morewood and Roberts,

223   1997). In this latter interpretation, the age of the marine terrace is suggested to be ~125 ka,

224   associated with MIS 5e (Morewood and Roberts, 1997; Roberts et al., 2009) (Figure 3b), with

225   the presence of complex faulting representing a Segment Boundary Zone between the EXFS

226   and SAFS. Both of these explanations rely on age constraints that link a wave-cut platform at

227   ~29 m to MIS 5e (125 ka highstand) dated using U-series coral ages (Vita-Finzi et al., 1993,

228   Leeder et al., 2003; Leeder et al., 2005; Houghton, 2010) (Locality F, Figure 4a), but no age

229   constraints have been available for higher elevation examples, and this is needed to

230   differentiate between the competing hypotheses.

231   We undertook detailed mapping and dating in an attempt to resolve the debate of

232   successive palaeoshorelines versus faults. In particular, we tried to identify whether the

233   slopes between terrace locations were continuous along strike, consistent with the

234   suggestion that they represent a succession of palaeoshorelines, or whether the offset of the

235   slopes varied along strike and displayed tip zones and relay ramps, suggestive of faulting.

236   Later we present the results of field mapping and dating that supports the hypothesis of

237   Morewood and Roberts (1997) that the observed variation in terrace elevation is as a result

238   of faulting.

239   The significance of Holocene wave-cut notches cut into the cliffs along the most

240   western point of Cape Heraion has also been the subject of debate (Pirazzoli et al., 1994;

241   Stiros, 1995; Stiros and Pirazzoli, 1998; Kershaw and Guo, 2001; Cooper et al., 2007; Boulton

242   and Stewart, 2015; Schneiderwind et al.,2017a; Schneiderwind et al.,2017b). It is clear that

243   these notches form as a result of the chemical, biological and physical wave action eroding

244   the cliffs in the intertidal zone along palaeoshorelines (Pirazzoli, 1986). The ages of four

245   notches observed on Cape Heraion were dated to between 190-440 A.D. and 4440-4320 A.D.

246   and used to infer coseismic footwall uplift increments of 0.8 m from earthquakes with

247   recurrence intervals of ~1600 years (Pirazzoli et al., 1994). However, 0.8 m has been

248   suggested to be a relatively high value for coseismic footwall uplift (Cooper et al., 2007;

249   Boulton and Stewart, 2015; Schneiderwind et al.,2017b; Meschis et al., 2019). Whatever their

250   mode of formation, we show below that the notches are deformed by active faulting and use

251   this as part of our explanation of the geological history of Cape Heraion.

252

253   2.3 *Using marine terraces and wave-cut platforms to obtain age constraints*

254   Exploring the deformation of marine terraces and wave-cut platforms relies on

255   obtaining age controls for terraces, accurate geomorphic mapping of terrace features and

256   knowledge of the timing and relative elevations of sea-level highstands (Robertson et al.,

257   2019). Existing coral ages on Cape Heraion at localities C, F and H (Figure 4a) dated using

258    $^{234}U/^{230}Th$ dating reveal ages that agree to coral growth during MIS 5e from platforms at 7 m

259   (Roberts et al., 2009), 29 m (Collier et al., 1992; Vita-Finzi et al., 1993; Leeder et al., 2003;

260   Leeder et al., 2005; Dia et al., 2007; Houghton, 2010) and 15 m (Burnside, 2010). To augment

261   these ages, this study provides new coral ages, and *in situ* [36]Cl cosmogenic exposure ages for

262   wave-cut platforms, inspired by the work of Stone et al. (1996), that can be mapped along

263   strike onto coral–bearing marine terrace sediments. The ^{36}Cl cosmogenic exposure ages are

264   cross checked against new and existing coral ages.

265   Integral to studies of Quaternary marine terraces and palaeoshorelines is knowledge

266   of sea-level elevation changes linked to sea-level highstands, and the time when sea-level

267   reached its maximum elevation (e.g. Waelbroeck et al., 2002; Lambeck et al., 2002; Siddall et

268   al., 2003; Grant et al., 2014; Spratt and Lisiecki, 2016). On Cape Heraion existing coral ages

269   constrain three wave-cut platforms to MIS 5e (125 ka sea-level highstand) (Localities C,F and

270   H, Figure 4a). The timing of MIS 5e occurred between 138-116 ka (Muhs and Szabo, 1994;

271   Stirling et al., 1998; Hearty et al., 2007; O'Leary et al., 2013; Dutton et al., 2015), with the

272   majority (80%) of sea-level rise suggested to have occurred prior to 135 ka (Muchs and Szabo,

273   1994; Gallup et al., 2002). Understanding the elevations and timings of past sea levels is

274   beneficial because it provides an additional check against the ages obtained from ^{36}Cl

275   exposure dating, which should fall within known highstand time periods.

276

277   3. **Methods**

278

279   *3.1 Field mapping*

280   Detailed field mapping and sampling for ^{234}U/^{230}Th and *in situ* ^{36}Cl exposure dating was

281   carried out during field campaigns throughout 2015 and 2017. For the field mapping we

282   concentrated on key criteria that would differentiate between the palaeo-sea-cliff versus fault

283   interpretations for the steep slopes between terrace locations. In particular, if the steep

284   slopes are palaeo- sea-cliffs they ought to be continuous along strike (Figure 3b). In contrast,

285   if the steep slopes are fault scarps, they may display relay-zone geometries where it would be

286   possible to walk continuously on a single surface, along strike, around fault tips, up relay

287   ramps onto the higher parts of the same terrace surface (Figure 3b).

288   In order to constrain the geometries and continuity of the marine terraces (Figure 3),

289   58 spot-height elevations were measured throughout the field area using a handheld

290   barometric altimeter (3 m vertical error) that was regularly calibrated at sea level. These

291   measurements were supplemented by 40 additional elevation values obtained from spot

292   heights from a 5 m digital elevation model (DEM) (4 m vertical error) in ArcGIS. The

293   combination of spot heights, outer edges and fault trace maps has allowed us to identify

294   displacement gradients, fault tips to individual faults and relay zones separating individual

295   faults. Rupture traces from recent (possibly 1981) faulting were mapped using a barometric

296   altimeter and measured with rulers to identify the vertical offsets (throw) observed in

297   colluvium and on bedrock fault scarps and the horizontal extension observed from piercing

298   points. This was carried out as per the approach outlined in Iezzi et al. (2018).

299

300   *3.2 $^{234}U/^{230}Th$ sampling approach and preparation*

301   We focussed our attention on a 0.5-1 m thick coral-bearing, bioclastic layer overlying

302   the bioherms. The bioclastic deposits are comprised of coarse sand and contain corallites of

303   *Cladocora caespitosa*. Whole corallite samples were removed and prepared as per the

304   approach outlined in Roberts et al. (2009). Each corallite sample was split and the septa

305   removed and discarded as septa have been shown to experience greater post-depositional

306   alteration (Roberts et al., 2009; Houghton, 2010). Individual samples were then fragmented

307   and analysed under a binocular microscope for signs of alteration that appear as patches of

308   brown colouration and small crystal growths. The corallites were physically cleaned using a

309   scalpel to remove areas of alteration and any sediment and then placed in 10% hydrochloric

310   acid for 2-3 seconds after which they were immediately rinsed in ultrapure water. This process

311   was repeated until all signs of alteration were removed. Following this process fragments

312   from each corallite were analysed for $^{234}U/^{230}Th$ as per the method detailed in Crémière et al.

313   (2016).

314

315   *3.3 ^{36}Cl sampling approach and preparation*

316   For ^{36}Cl dating we focussed our attention on wave-cut platforms that could be mapped

317   along and across strike into the coral-bearing, bioclastic layer, suggesting they would be close

318   in age. Obtaining the absolute ages of wave-cut platforms using cosmogenic ^{36}Cl exposure

319   dating relies on (i) sampling from a surface comprised of a calcium-rich lithology that has (ii)

320   experienced minimal erosion and negligible burial, under soil for example, since exposure.

321   This is because the primary production pathway of cosmogenic ^{36}Cl occurs when ^{40}Ca

322   undergoes spallation following the collision of high-energy neutrons at the earth's surface

323   (Dunai, 2010). The spallation reaction is mostly limited to the upper 2 m of rock below

324   exposed surfaces, decreasing exponentially with depth (Licciardi et al., 2008), so high levels

325   of erosion would remove the highest concentrations producing misleadingly-young ages.

326   Other pathways of ^{36}Cl production that must be considered are from low-energy neutrons

327   (Schimmelpfennig et al., 2009) and negative muons, which are the dominant production

328   mechanism for ^{36}Cl at greater depths (Dunai, 2010). We use the approach outlined in

329   Robertson et al. (2019) to identify surfaces that have experienced minimal erosion based on

330   the presence of preserved lithophagid borings and millholes. The depth of lithophagid borings

331   upon formation is between 3-9 cm (Peharda et al., 2015) while millholes, that is, erosional

332   hollows formed by pebble agitation in the intertidal zone, are usually a few centimeters to

333   less than a few decimetres deep. Therefore, the preservation of these features allows us to

334   be confident that we can constrain erosion to less than a few millimetres or centimetres. The

335   low rates of erosion mean that the ^{36}Cl concentration depth profile, determined by the ^{36}Cl

336   production rate depth variation from spallation, will be intact and amenable to age derivation

337   using modelling.

338   We sampled from wave-cut platforms comprised of differing lithologies at a range of

339   elevations: 62 m, 60 m, 46 m, 42 m and 29 m, including one location where there is an existing

340   age control from ^{234}U/^{230}Th coral ages (Locality F, Figure 4a) from sediments formed quasi-

341   contemporaneously with the wave-cut platform (Vita-Finzi et al., 1993; Leeder et al., 2003;

342   Leeder et al., 2005; Houghton, 2010). All samples were removed using a mallet and chisel.

343   Shielding values were noted every 30° of azimuth (as per the method in Dunai, 2010), and

344   used in the age exposure calculations to account for the shielding of cosmogenic rays on the

345   sample site by the surrounding topography (Dunai, 2010). Following removal, samples were

346   analysed in thin section to determine their lithology, washed in distilled water in an ultrasonic

347   bath, then crushed and prepared for ^{36}Cl exposure dating using Accelerator Mass

348   Spectrometry (AMS) as per the method outlined by Schimmelpfennig et al. (2009). The data

349   obtained from AMS was input into CRONUScalc (Marrero et al., 2016), an online calculator

350   that uses measured inputs from data such as ^{36}Cl concentration, elemental composition,

351   elevation, shielding, water content and appropriate uncertainties to calculate the age of the

352   samples with uncertainty values attached.

353

354   4. **Results**

355

356   This section explores the results of our detailed geological mapping of Cape Heraion

357   and the absolute ages obtained from our ^{36}Cl cosmogenic exposure dating and ^{234}U/^{230}Th

358   dating. Alongside existing published ages, these new absolute ages are used to constrain the

359   ages of surfaces at different elevations on Cape Heraion in order to show that faulting is

360   responsible for offsetting a marine terrace linked to the 125 ka highstand within MIS 5e. The

361   results of the dating are used to drive throw rate analyses in order to calculate cumulative

362   throw within the tip zone since 125 ka.

363

364   *4.1 Field mapping*

365   Detailed field mapping reveals complicated, but linked spatial relationships between

366   lithologies, the stratigraphy and geomorphic features on Cape Heraion (Figures 4, 5,

367   Supplementary data 1, which contains a description of the stratigraphy). Wave-cut platform

368   features have been cut into the stratigraphy (Figure 4a) and are widespread throughout the

369   cape at elevations from 6 m to 99 m (Figures 4, 5 and 6). These horizontal to sub-horizontal

370   surfaces exhibit millholes and lithophagid borings, which are particularly well preserved on

371   the platforms composed of bioclastic packstone (Figures 4a, 6f). Associated with the wave-

372   cut platforms, several localities display coastal notches where the wave-cut platforms

373   impinge on steep outcrops. The notches are marked with lithophagid borings, for example

374   close to location B at ~41 m, with another notch observed at ~92 m (Locality J, Figure 4a).

375   Our mapping suggests that the lithologic, the stratigraphic and geomorphic features

376   can be interpreted as due to the effect of wave-erosion, at the time of wave-cut platform

377   formation, impinging on palaeo- Cape Heraion, characterised at that time by Quaternary

378   sediments onlapping onto an upstanding inlier of Mesozoic limestone (Figure 5b). The lateral

379   stratigraphic variations were denuded by the wave erosion so that the wave cut-platform

380   formed on different stratigraphic units across the mapped area. The stratigraphy, and the

381   wave-cut platform, have been subsequently offset by faulting that, therefore, post-dates the

382   wave-cut platform, the Cladocora-bearing bioclastic sands and the Rivularia-bioherms (Figure

383   7).

384   To gain further insights into the faulting, we have studied the steep slopes that occur

385   along the faults, and in particular the breaks of slope (Figure 4a, c). The map pattern produced

386   by the breaks of slopes reveals patterns that resemble displacement variations along the

387   faults, with slip maximum close to the centres of the map traces, and the positions of relay-

388   ramps at fault tips (Figure 4c). Hence, we interpret these breaks of slope to represent

389   hangingwall and footwall cut offs. Cross-sections across the faults are shown in Figure 8. To

390   cross-check the interpretation of fault segmentation in Figure 4c, we used the elevation data

391   shown in Figure 4b to measure the vertical offsets across the faults, checking that relay-ramps

392   and fault tips identified on Figure 4c are marked by decreased vertical offsets (Figure 9). This

393   cross-check confirms that locations where the hangingwall and footwall cut-offs converge in

394   map view (e.g. the relay-ramps and faults tips in Figure 9b) have low or zero vertical offsets,

395   consistent with our fault segmentation model.

396   As a final check on the geometries of the faults we have compared their displacement

397   (d) to length (L) ratios to those in a global database (Schlische et al. 1996), because $d = \gamma L$,

398   where γ = 0.01-0.1 with a preferred value of 0.03. We have analysed faults where we have

399   identified both fault tips, and faults where we consider that the centre of the fault has been

400   mapped, assuming that the displacement profiles will be symmetrical. We find values of

401   γ between 0.01-0.1 (Table 1), suggesting that the vertical extents of the steep slopes

402   separating terrace locations are consistent with the interpretation that they are fault scarps.

403   The exception is fault 4, which has a d/L ratio that is comparatively higher (0.27), possibly as

404   a result of being linked at depth with faults 1 and 10 (see the individual fault throw profiles in

405   Figure 9a for faults 1, 4 and 10). Consequently, the combined d/L ratio of these three faults is

406   not representative because the fault continues offshore to the west (Figure 4a, b).

407   We describe the details of the faulting below. With the exception of three faults that

408   strike approximately N-S not considered in this study, all of the faults strike parallel-sub

409   parallel to the average 260° of the SAFS between 230° and 300° (Figures 2, 4). The faults in

410   the north of the cape are all north dipping and exhibit short fault lengths (100-400 m) and

411   offsets of 2-20 m. South of Fault 11 the presence of a north dipping fault is inferred owing to

412   the 20 m offset of bioherms observed along the scarp of fault 11 (Figure 4a, b). Faults along

413   the south of the cape are longer, and extend outside of the mapping area to the east and

414   offshore to the west (faults 1, 17 and 18) (Figures 4a-c, 7a-c). Along the south of the cape,

415   there are four south-dipping faults (1, 4, 10 and 18) (Figures 4b, 7a-c, e, f). The scarp of fault

416   18 is not accessible and the offset of this fault is a minimum value as its hangingwall is

417   offshore, however, this fault has been mapped by Morewood and Roberts (1999) farther to

418   the east for ~2 km. South dipping faults 1, 4 and 10 appear to be en echelon to one another

419   and exhibit limestone fault scarps that decrease in offset from west to east.

420   Strike and dip values, and, where visible, fault striations were measured along the

421   limestone fault scarps of Faults 1, 2, 10 and 17 (Figure 4d). The fault dip for these faults range

422   between 43-66°. In places faults display evidence of activity in a marine setting, faults 1 and

423   4 display post-slip marine cementation of submarine screes coating the faults (Scott, 1995).

424   Along north dipping faults 2 and 11, offset algal bioherms have horizontal lines of abundant

425   lithophagid borings at 34 m and 41 m respectively, again suggesting slip pre-dates wave-cut

426   platform formation.

427   In summary, our geomorphological observations and elevation measurements

428   suggest that a pattern of distributed faulting is visible on Cape Heraion. In the context of the

429   north-dipping SAFS and its approximate E-W strike, the faulting on Cape Heraion displays a

430   set of synthetic and antithetic faults that display a 70° variation in strike. While north-dipping

431   faults are more numerous, they appear to have smaller lengths and offsets compared to the

432   four south dipping faults.

433

434   *4.2 ^{234}U/^{230}Th coral dating*

435   The *Cladocora caespitosa* corallites sampled from Cape Heraion (S6U/Th, S7U/Th)

436   (Figure 4) were removed from within a death assemblage on the 44 m wave-cut platform

437   predominantly composed of friable sediments (Figures 6c, 7a). Results of ^{234}U/^{230}Th dating on

438   S6U/Th and S7U/Th reveal growth ages of 137 ka and 136 ka respectively (Figure 8a, Table 2).

439   The age presented for S6U/Th is comprised of the average of three analyses from the same

440   corallite, a fourth age was also obtained from this corallite, but we have excluded it as the

441   age of 173.7 ky suggests that it is an outlier and not representative of the age of the corallite

442   (Table 2). The average age of sample S7U/Th is obtained from six analyses from the same

443   corallite (Table 2). The ^{234}U/^{230}Th coral ages support growth during MIS 5e and are similar to

444   existing coral growth ages from Cape Heraion (Figure 8a; Vita-Finzi et al., 1993; Leeder et al.,

445   2005; Roberts et al., 2009; Burnside, 2010; Houghton, 2010). Note that all samples have

446   relatively high values of δ^{234}U of 191-214 (a common way to represent the initial activity ratios

447   of ^{234}U/^{238}U) compared to modern seawater in the Gulf of Corinth (value of 151; Roberts et

448   al., 2009). It is expected that the samples should have δ^{234}U values similar to modern sea-

449   water. However, previous studies of coral ages in the Gulf of Corinth, which successfully

450   produced ages of independently-known glacio-eustatic sea-level highstands, have tended to

451   show elevated values (e.g. Collier et al., 1992; Vita-Finzi et al., 1993; McNeill and Collier, 1994;

452   Dia et al., 1997; Leeder et al., 2005; Roberts et al., 2009; Burnside, 2010; Houghton, 2010;

453   Turner et al., 2010), probably due to the fact that it is a restricted basin with freshwater input.

454   The analyses herein also suggest an age similar to a well-known glacio-eustatic sea-level

455   highstand at ~125 ka. Thus, like previous studies, we use the implied age in our later analysis,

456   despite the relatively high initial activity ratio for our samples.

457

458   *4.3 ^{36}Cl exposure dating of wave-cut platforms*

459   Cosmogenic ^{36}Cl exposure dating is employed to calculate the time period that

460   sampled surfaces have been subaerially exposed and thus accumulating significantly higher

461   values of ^{36}Cl compared to pre-exposure. Five samples were removed from limestone,

462   bioclastic packstone and algal bioherm wave-cut platforms at different elevations on Cape

463   Heraion (Figures 4a, 6). Our field observations are used to inform the erosion rate used as an

464   input parameter into CRONUScalc, which is used to calculate the exposure age of the samples

465   (see Supplementary data 2 for CRONUScalc input data). The preservation of lithophagid

466   borings and millholes on bioclastic packstone and limestone surfaces (samples 1 and 3)

467   (Figure 6b, f) indicate total erosion values of less than 0.2-0.3 m, whilst samples from the tops

468   of bioherms (samples 2, 4 and 5) are expected to have experienced total erosional values

469   similar with the removed depth of bioclastic packstone/grainstone eroded from the surface

470   of ~0.6 m. These limestone/packstone and bioherm values equate to erosion rates of 0.1 and

471   ~6.0 mm/ky respectively. We note that the 0.1 mm/yr value is the same as that used on

472   limestone wave-cut platforms dated using ^{36}Cl exposure dating in south Crete (Robertson et

473   al., 2019).

474   Assuming the erosion rates stated above are correct, the ^{36}Cl exposure ages of five

475   samples (Figure 8a, Table 3) are: S1 (limestone, sampled at 60 m) 122 ± 29 ka; S2 (bioherm,

476   sampled at 62m) 108 ± 36 ka; S3 (bioclastic packstone, sampled at 42 m) 109 ± 24 ka; S4

477   (bioherm, sampled at 46 m) 120 ± 40 ka; S5 (bioherm, sampled at 29 m) 112 ± 35 ka. These

478   results agree with the new and existing U-series ages presented above, suggesting late

479   Quaternary ages close to the age of the 125 ka highstand. The error bars on the ages appear

480   relatively-large, but are comprised of internal (analytical) and external (total) uncertainties

481   that are associated with measured input parameters into CRONUScalc (e.g. H_2O content,

482   elevation, shielding, erosion rates and the production rate; Marrero et al., 2016). Where

483   samples are removed from the same geographical location using the same method, the error

484   values of the input parameters used to calculate the external uncertainty will be very similar

485   (i.e. shielding) or even the same (i.e. production rate, elevation values). Consequently,

486   Marrero et al. (2016) suggests that the external uncertainty value linked to the exposure age

487   may be overestimated when comparing results from the same geographical area, sampled

488   using the same method (see Dunai, 2010). This possible overestimate of uncertainties should

489   be borne in mind when considering the relatively-large error bars associated with the

490   exposure ages, but we have chosen to report the external uncertainties herein.

491   While the erosion rates used to calculate exposure ages are based upon field

492   observations, we recognise that they form an uncertainty in the ages obtained. Therefore, we

493   examine the sensitivity of the exposure age results to uncertainties in the estimated erosion

494   rates. For samples 1 and 3, we tested erosion rates from 0.1-1 mm/ky and for samples 2, 4

495   and 5 we tested erosion rates from 5.5-6.5 mm/ky (± 0.5 mm/ky of our estimated erosion

496   rates). The results of these analysis (Supplementary data 3) reveal that the exposure ages may

497   all be allocated to the 125 ka highstand even if our chosen erosion rate is adjusted within the

498   range of ± 0.5 mm/ky. Values for erosion rate larger than this would not be consistent with

499   our field observations of features such as preserved millholes and lithophagid borings. We

500   therefore suggest maximum and minimum values for rates of erosion for samples 1 and 3 of

501   0.1-1 mm/ky and for samples 2, 4 and 5 of 5.5-6.5 mm/kr. These results support our

502   contention that our erosion rate estimates (samples 1, 3: 0.1 mm/ky and samples 2, 4 and 5:

503   6 mm/ky) are acceptable.

504   We suggest that all our exposure ages for the wave-cut platform are associated with

505   MIS 5e, and we discuss this below. Our exposure age results link S1 and S4 and their

506   associated wave-cut platforms to MIS 5e, but the wave-cut platforms that S2, S3 and S5 were

507   removed from, might, at first sight, be linked to either MIS 5c (100 ka highstand) or MIS 5e

508   (125 ka highstand) (Figure 8a). However, using the exposure ages obtained from S1 (60 m)

509   and S4 (46 m), new $^{234}U/^{230}Th$ ages from S6 and S7 (44 m) and existing U-series dating of corals

510   on platforms at 7 m (Roberts et al., 2009), 15 m (Burnside, 2010) and 29 m (Vita-Finzi et al.,

511   1993; Leeder et al., 2003; Leeder et al., 2005; Houghton, 2010) alongside sea-level curve data

512   we suggest that it is more likely that S2 (62 m), S3 (42 m) and S5 (29 m) are associated with

513   MIS 5e (Figure 8c). Our reasoning is that it is difficult to reconcile that platforms at 60 m, 46

514   m, 44 m, 29 m, 15 m and 7 m were formed by the MIS 5e 125 ka highstand, yet platforms at

515   similar elevations (62 m, 46 m and 29 m) were formed by the MIS 5c 100 ka highstand. This is

516   especially unlikely, given that the maximum sea level during the 100 ka highstand in MIS 5c

517   was -25 m relative to today, and this is 30 m lower than the 5 m relative sea level during the

518   125 ka highstand of MIS 5e (Siddall et al., 2003) (Figure 8a).

519   The results of our dating, combined with existing age controls and detailed geological

520   mapping strongly supports that the observed wave-cut platforms on Cape Heraion were all

521   formed during the 125 ka highstand of MIS 5e and have been subsequently faulted since this

522   time (Figure 8c).

523

524   *4.4 Holocene displacements*

525   Offset Holocene notches and surface faulting that may be associated with the 1981

526   earthquake suggest occurrence of Holocene faulting on Cape Heraion (Figure 7). An offset

527   notch exists along the base of a cliff at the south west of the cape of as a result of slip on Fault

528   1 (Figures 4b, 7b). The highest notch is offset by 1.08 m between the footwall and the

529   hangingwall, but it does not appear that a lower notch is also offset (Figure 7b). Our

530   explanation for this is that faulting occurred on Fault 1 following the formation of the upper

531   notch between 4440-4320 B.C. (Pirazzoli et al., 1994) prior to the formation of the lowest

532   notch (at ~1.4 m) between 440-190 A.D.; this may be interpreted as evidence of Holocene

533   faulting on this part of the cape.

534   Evidence of recent surface faulting may also be present on the north of the cape as a

535   several metre-deep fracture offsetting the bioherms. The fracture (Locality I Figure 4a, and

536   Figure 7d) has a strike of 245°, a horizontal offset of 43 cm, and a direction of opening of 332°,

537   as measured by matching piercing points on both hangingwall and footwall. On Fault 17

538   between localities J and K (Figure 4a), the occurrence of surface faulting is suggested by a

539   fresh, lichen-free stripe at the base of a carbonate fault plane. These possible surface

540   ruptures, if extrapolated along-strike, cover a distance of ~300 m along the faults. Between

541   localities J and K we observed seven locations that display fresh lichen-free stripes on bedrock

542   fault planes (Figure 7e and f). Bedrock offsets (measured as vertical throw) appear as a light

543   grey stripe at the base of a free face, preserving what appears to be the relative coseismic

544   movement of the colluvium along the fault rupture, ranging from 3-12 cm of throw. In places,

545   the surface rupture has also stepped forward into the hangingwall, located a few centimetres

546   to decimetres away from the carbonate fault plane, to offset the hangingwall colluvial

547   deposits (Figure 7e); vertical offset in the colluvium ranges between 7-28 cm, measured at

548   eight locations between localities J and K (Figure 4a).

549   As the 1981 earthquakes are the most recent to result in surface ruptures on the Pisia

550   fault (Jackson et al. 1982; Taymaz et al., 1991; Hubert et al., 1996; Roberts, 1996a), and

551   ruptures were reported as close by as along the shore of Lake Vouliagmeni (Bornavas et al.

552   1984; Figure 2c), we suggest that it is plausible that the ruptures on Cape Heraion, may have

553   also occurred coseismically during the 24th and/or 25th February 1981 earthquakes.

554

555   *4.6 Throw rates and uplift rates*

556   The absolute ages of wave-cut platforms gained in this paper constrain their formation

557   to the 125 ka highstand within MIS 5e. This means that we can quantify the throw-rate and

558   uplift-rates since 125 ka (Figure 9) to the present day. To constrain the fault geometries, we

559   used elevation data for the footwall and hangingwall cut-offs along the strike of fault traces

560   from the geological and geomorphological map (Figure 4) to construct throw profiles across

561   each fault. Plots of the individual throws for all faults show that faults have maximum offset

562   values of <40 m with two faults exceeding this value (17 and 18) (Figure 9a). When all of the

563   fault throw values and rates are summed across strike they show a pattern of decreasing

564   displacement from east to west (Figure 9c). We emphasise that the data in the grey area on

565   Figure 9c should be interpreted with more caution due to the lack of absolute age control

566   obtained for the wave-cut platform located in the footwall of fault 17 (Figures 4a, 9a), but

567   here we infer that if the notch and small wave-cut platform at ~92-99 m (Locality J, Figure 4a)

568   cut into the footwall of Fault 17 represents the 125 ka palaeoshoreline (Figure 8c, profile 3),

569   we can constrain the throw rate, and we include this in our summed values.

570   When fault throw and throw rates are plotted separately for the north- and south-

571   dipping faults they mirror the pattern of summed values decreasing from east to west (Figure

572   9c). It is interesting to note that four south-dipping faults accommodate more throw

573   compared to 14 north-dipping faults with the exception between 1900-1800 m to the west of

574   the 'on fault' throw minima (Figure 9c). We postulate that this may be a reflection of the

575   broader faulting pattern within the Gulf of Corinth where the polarity of faulting switched

576   from south-dipping faults to north-dipping faults during the late Quaternary (Roberts et al.,

577   2009; Nixon et al., 2016). Specifically, Roberts et al. (2009) suggested that the north-dipping

578   SAFS experienced an increase in slip at ~175 ka. The short fault lengths and small

579   displacements of the north dipping faults on Cape Heraion may indicate that they may be less

580   mature compared to their south-dipping counterparts. As the summed throw values do not

581   decrease to zero in the mapped area, we suggest that the point of zero vertical offset may lie

582   offshore to the west of Cape Heraion, unless the faulting is actually hard-linked to offshore

583   EXFS.

584   Another way to consider the results is to explore how throw across active faults has

585   produced spatial variation in uplift relative to present-day sea-level. In other words, the

586   absolute ages of wave-cut platforms, and knowledge of their elevations, allows calculation of

587   spatial variation in uplift rates since 125 ka. Uplift rates since 125 ka from the highest and

588   lowest dated wave-cut platforms are calculated as 0.46 mm/yr (S2, 62 m) and 0.02 mm/yr

589   (Sample P1CWall, 7 m, Roberts et al., 2009) respectively (Figure 4a). If our assertion that the

590   observed notch at 92 m (Locality J, Figure 4a) marks the palaeoshoreline of the 125 ka is

591   correct then a maximum uplift rate of 0.7 mm/yr on Cape Heraion is derived using the 92 m

592   elevation (N.B. these calculations take into account that the sea-level elevation of the MIS 5e

593   highstand was +5 m relative to today's sea-level). The extreme variability in uplift rate over

594   distances of tens of metres or less precludes simple interpretations of regional tectonic signals

595   in our opinion, as the local uplift is clearly dominated by local faulting (c.f. Leeder et al. 2005).

596   While the ages obtained in this study and the existing coral U-series link the formation

597   of the wave-cut platforms to the MIS 5e highstand, field observations suggest that some faults

598   were already active prior to MIS 5e. Evidence for this is in the form of (a) marine cementation

599   within submarine screes coating the fault planes on Faults 1 and 4, (b) stratigraphic variations

600   across faults in and below the bioherms, and (c) flat-topped bioherms in the footwall versus

601   domed-topped bioherms in the hangingwall that are suggested to have grown up toward

602   water surface levels during formation (Figure 5) (also observed by Kershaw and Guo, 2006).

603   This evidence suggests that faulting on Cape Heraion was active prior to the beginning of the

604   MIS 5e (~138 ka) and continued throughout the marine stage and beyond. It is possible that

605   along the faults with smaller offsets (such as those in the north) any coseismic offset prior to

606   125 ka may have either been consequently covered by syn-wave-cut platform sediments or

607   eroded prior to or during the formation of the 125 ka platform; this is particularly plausible

608   given that between the start of MIS 5e at ~138 ka and the highstand at 125 ka any fault offset

609   on the peninsula over this time would have been subject to the erosive forces of rising sea

610   level. Furthermore, coseismic offsets on the faults on the peninsula are expected to be

611   relatively small (a few cm) and therefore easier to erode or obscure with sediment.

612

613   5. **Discussion**

614   Detailed fault mapping and absolute dating on Cape Heraion reveals that the western

615   tip zone of the SAFS accommodates deformation via distributed faulting along synthetic and

616   antithetic faults. Importantly, our findings provide evidence of faulting during the Late

617   Quaternary, specifically over decadal, 10^3 and 10^5 year timescales that is ongoing into the

618   Holocene and perhaps even as recently as 1981. Offset marine terraces and their wave-cut

619   platforms throughout the entire mapped area can be linked to the 125 ka highstand within

620   MIS 5e. The findings presented in this study, therefore, provide evidence of significant late-

621   Quaternary faulting on Cape Heraion. This outcome is in direct contrast to the findings of

622   Leeder et al. (2003) and Leeder et al. (2005) who refute the notion of displacement of

623   Holocene and late Quaternary shoreline deposits within the study area, and conclude that the

624   Perachora Peninsula is uplifting at a constant, low, uniform rate of 0.2-0.3 mm/yr possibly

625   linked to angle of dip of the subducting African plate beneath the eastern Gulf of Corinth

626   (Leeder et al., 2005) and representing a 'background' uplift rate for the region.

627   Our fault throw analyses show that summed throw rates in the tip area appear to be

628   relatively high, up to ~1.6 mm/yr (Figure 9), compared to throw and slip rates near the centre

629   of the Pisia and Skinos faults of up to 2.3 mm/yr (Mechernich et al., 2018) and 0.7-2.5 mm/yr

630   (Collier et al., 1998) over the Holocene and 1.2-2.3 mm/yr over the longer term (Collier et al.,

631   1998). From the findings presented here, we conclude that detailed across strike mapping

632   within the tip zone of a fault is imperative in order to constrain accurate rates of long-term

633   faulting that could otherwise be underestimated. We show that the tips of faults should be

634   considered as zones of deformation, rather than localised surface features where a fault stops

635   as they contain multiple active faults.

636

637   5.1 *High throw rates on Cape Heraion*

638   Our findings lead us to question why the throw values obtained in the western tip

639   zone over 125 ka are anomalously high compared to those observed along the localised fault

640   (Figure 10a). Studies of tip displacement gradients commonly suggest high gradients occur

641   where the tips of two faults overlap, as a consequence of the interaction between the stress

642   fields of the faults (e.g. Peacock and Sanderson, 1991; Huggins et al., 1995; Willemse et al.,

643   1996; Cartwright and Mansfield, 1998; Cowie and Shipton, 1998; Gupta and Scholz, 2000;

644 Ferrill and Morris, 2001; Scholz and Lawler, 2004; Fossen and Rotevatn, 2016). Analysis of an

645 isolated fault tip by Cowie and Shipton (1998) revealed an average tip displacement gradient

646 of 0.018, whereas Cartwright and Mansfield (1998) obtained gradients between 0.0164 to

647 0.25, in their study of 20 normal faults comprised of a mixture of isolated and interacting

648 faults. In comparison, the tip displacement gradient for the investigated western tip zone of

649 the SAFS is 0.233 (Figure 10b), at the upper range of those observed above.

650 An explanation of the relatively high summed throw rates on Cape Heraion may be

651 due to fault interaction between the stress fields of the EXFS and the SAFS located along strike

652 to one another and whose eastern and western fault tips overlap (Figure 2a). While this

653 suggestion has been proposed by Morewood and Roberts, (1997), it has not been

654 quantitatively investigated. One way of exploring fault interaction between overlapping faults

655 relies on modelling the calculated Coulomb stress transfer from rupturing a source fault onto

656 a receiver fault. Studies of Coulomb stress transfer (King et al., 1994; Toda et al., 2005) show

657 that following an earthquake, changes in the stress around the slipping patch on the source

658 fault occur that may influence seismicity on neighbouring receiver faults, with positive

659 Coulomb stress transfer bringing a receiver fault closer to failure and negative Coulomb stress

660 transfer resulting in stress shadows. The presence of a stress shadow on the tip zone of a

661 receiver fault may result in deceleration of the propagation of the tip of the receiver fault,

662 which consequently results in displacement accumulating near its interacting tips, causing

663 steeper displacement gradients (Gupta and Scholz, 2000, Figure 14). The deceleration occurs

664 because the fault at the interacting tip must overcome the rupture resistance and stress drop

665 imposed by the adjacent fault (Walsh and Watterson, 1991; Scholz and Lawler, 2004).

666 We explore whether the location of the eastern EXFS tip zone (Figure 2a) could perturb

667 the stress field of the western tip zone of the SAFS by modelling the Coulomb stress changes

668 following an earthquake on the EXFS (source fault) onto the SAFS (receiver fault) using

669 Coulomb 3.3.01 software. We use the approach and updated code of Mildon et al. (2016)

670 within Coulomb 3.3.01 that allows strike-variable faults to be used, as Coulomb stress transfer

671 is particularly sensitive to changes in the strike of receiver faults (Mildon et al., 2016). An

672 accurate fault trace drawn using Google Earth^{TM} and geometries (dip, strike, rake) of the

673 source (EXFS) and receiver (SAFS) faults (Table 4) were input into the code from Mildon et al.

674 (2016). The source fault was then ruptured to produce a 'standard' earthquake, determined

675 using fault-scaling relationships to calculate the maximum magnitude from the length of the

676 fault rupture (Wells and Coppersmith, 1994). Three source fault rupture scenarios are

677 modelled: (1) the rupture of the SAFS with the exception of the western 2.5 km of the SAFS;

678 (2) the rupture of the entire EXFS; (3) a partial rupture of the EXFS, which involves only the

679 most eastern segment (the Perachora fault) (Figure 2a). Scenario (1) was modelled in order

680 to establish the Coulomb stress transfer imparted from a partial rupture of a fault onto its

681 own tip area (e.g. Roberts 1996). Note that within the Coulomb stress transfer scenarios, the

682 western tip area of the SAFS is defined as the western 2.5 km section of the SAFS, from Point

683 A (Figure 2a) to the west tip of Cape Heraion.

684   The results of Coulomb stress transfer modelling show stress enhancement on the

685 shallow portions of faults in the region of Cape Heraion, or stress enhancement to greater

686 depths, depending on the exact source to receiver geometry. Rupturing the entire SAFS with

687 the exception of the western 2.5 km section (Scenario 1), results in a significant positive

688 Coulomb stress change of 2 bars onto the entire fault plane of the SAFS western 2.5 km

689 section (Figure 11b). Rupturing the entire EXFS (Scenario (2)) results in the upper and lower 2

690 km of the SAFS western 2.5 km section experiencing positive stress transfer of 2 bars, while

691 the majority of the western 2.5 km section of the fault plane displays negative stress transfer

692 of up to -2 bars (Figure 11c). Similarly, in scenario (3), rupturing only the Perachora fault

693 segment of the EXFS also results in negative stress transfer of -2 bars over almost all of the

694 western 2.5 km section of the fault with the exception of the upper 1 km, which experiences

695 positive stress transfer values of 1-2 bars (Figure 11d). Overall, the high values of

696 displacement observed on Cape Heraion over 125 ka may be explained by fault interaction

697 between the overlapping tips of the EXFS and the SAFS.

698

699 5.2 *Impacts on seismic hazard*

700 Our findings have implications for fault-based probabilistic seismic hazard assessment

701 (PSHA). We show here that the tip zone of a crustal-scale normal fault can accommodate

702 significant displacement 'off the localised fault', possibly linked to interaction with a

703 neighbouring fault. If these patterns of deformation are assumed to be typical for other

704 normal crustal-scale faults within fault systems that overlap along strike, such as those in the

705 Central and Southern Italian Apennines (Roberts and Michetti, 2004; Papanikolaou et al.,

706 2005; Papanikolaou and Roberts, 2007; Iezzi et al., 2019) and Basin and Range Province,

707 Western USA (e.g. Machette et al., 1991; Anders and Schlische, 1994; Schlische and Anders,

708 1996, *and references therein*) then our findings may help shed light on how to incorporate

709 slip/throw values into regional datasets, and whether displacements can jump from one

710 major fault to another.

711 It is known that measurements of slip rate are key inputs into PSHA calculations to

712 gain recurrence intervals and probability of shaking events (e.g. Boncio et al., 2004; Pace et

713 al., 2010; 2016; Valentini et al., 2017). However, due to a sparsity of data, it is common to

714 extrapolate slip rate data from measurements collected on a single location along a fault. This

715 is predominantly done by assuming that displacement decreases towards fault tips (Faure

716 walker et al., 2018). The present study shows that this approach can be problematic, because

717 the interaction between overlapping and interacting fault tips of neighbouring faults might

718 result in anomalously-high displacement in the tip zone, so that throw and slip rates do not

719 simply decrease along strike. Thus, calculation of recurrence rates and the probabilities of

720 given shaking intensities may be in error in such situations.

721   If our suggestion that high values of displacement in the overlapping tip zones

722 between the EXFS and the SAFS are as a result of fault interaction is correct, then the

723 possibility that earthquake ruptures may jump between the EXFS and SAFS should also be

724 explored. Fault interaction has the capacity to affect rupture sequences whereby seismic

725 events may 'jump' across interacting faults, causing multi-fault earthquakes (e.g. Gupta and

726 Scholz, 2000; Iezzi et al., 2019). For instance, from analysis of the source parameters of the

727 1981 earthquake sequence, Abercrombie et al. (1995) suggested that the 1981 earthquake

728 sequence might represent a multi-fault rupture between the SAFS and EXFS (or a segment of

729 the EXFS), during which the rupture might have originated offshore and propagated eastward

730 onshore. However, this analysis was carried out without consideration of the distributed

731 faulting reported herein. It is beyond the scope of this paper to confirm or deny whether the

732 presence of distributed faulting may make jumps between co-located faults more or less

733 likely. However, this topic is important because the recent UCERF 3 model (Field et al., 2017)

734 recognises the potential of ruptures to jump between faults that are co-located along strike

735 separated by small distances (5 km), a value similar to those identified by empirical studies of

736 normal faulting earthquakes between 5-7 km (e.g. DePolo et al., 1991; Wesnousky, 2008). The

737 maximum step between the SAFS and EXFS is ~4 km (Figure 2), within the values reported

738 above. Moreover, the observation that anomalously high displacement has accumulated in

739 the Cape Heraion tip zone may be evidence that earthquake ruptures do cross the tip zones,

740   but their presence is only detected if detailed mapping is conducted, and excellent age

741   constraints are available to gain rates of deformation.

742   We contrast the wealth of observations we provide in the Cape Heraion tip zone with

743   the more typical situation away from sea-level, where transverse bedrock ridges tend to

744   occupy tip zones, and these ridges are made of uniform pre-rift lithologies. In these locations,

745   sparse Quaternary or Holocene sediments may make it difficult to study and gain evidence

746   for active faulting and rates of deformation (e.g. Roberts and Koukovelas, 1996, elsewhere in

747   central Greece; Roberts and Michetti, 2004, Italian Apennines; Zhang et al., 1991; Crone and

748   Haller, 1991; Wu and Bruhn, 1994 western USA, for examples of such transverse bedrock

749   ridges). It may be that smaller distributed displacements remain undiscovered in tip zones

750   between major active faults, and this warrants more investigation, because their study may

751   be one of the few ways to observe whether ruptures cross tip zones to produce hazardous,

752   multi-fault earthquakes.

753

754   **6. Conclusions**

755

756   1. Cape Heraion, in the western tip zone of the South Alkyonides Fault System, deforms via a

757   set of distributed faults that are synthetic and antithetic to the 'main fault' and have been

758   active over decadal, 10^3 yr and 10^5 yr timescales. New age constraints using ^{36}Cl cosmogenic

759   exposure dating and ^{234}U/^{230}Th age dating of corals reinforce that the marine terraces and

760   associated wave-cut platforms on Cape Heraion are linked to the 125 ka highstand within MIS

761   5e rather than a set of terraces from three successive MIS phases.

762   2. On Cape Heraion, summed throw values (211 – 35 m), throw rates (1.68 – 0.25 mm/yr) and

763   uplift rates (maximum 0.7 mm/yr) appear to exceed those reported on the main fault. These

764 deformation rates are reflected in an anomalously high displacement gradient of 0.233.

765 Coulomb stress change modelling suggests that this is a consequence of the fault interaction

766 between the overlapping tips of the EXFS and the SAFS.

767 3. Our findings have implications for probabilistic seismic hazard calculations as they show

768 that the tip zones of crustal-scale faults may host high deformation rates caused by

769 distributed faulting and as such should be mapped in detail across strike. This is particularly

770 important for fault systems worldwide where crustal-scale faults may over lap and where the

771 slip rates are typically propagated along strike from one or two measurements assuming a

772 fault that linearly decreases to zero at the tips.

773

783

784 Abercrombie, R. E., Main, I. G., Douglas, A., & Burton, P. W. (1995). The nucleation and
785 rupture process of the 1981 Gulf of Corinth earthquakes from deconvolved broad-band
786 data. *Geophysical Journal International*, *120*(2), 393-405.

787 Anders, M. H., & Schlische, R. W. (1994). Overlapping faults, intrabasin highs, and the
788 growth of normal faults. *The Journal of Geology*, *102*(2), 165-179.

789 Andrews, J. E., Leeder, M. R., Portman, C., Rowe, P. J., Smith, J., Kershaw, S., & Guo, L.
790 (2007). Discussion on Pleistocene calcified cyanobacterial mounds, Perachora peninsula,
791 central Greece: a controversy of growth and historyGeological Society, London, Special
792 Publications, Vol. 255, 2006, 53–69. *Journal of the Geological Society*, *164*(5), 1065-1072.

793 Armijo, R., Lyon-Caen, H., & Papanastassiou, D. (1991). A possible normal-fault rupture for
794 the 464 BC Sparta earthquake. *Nature*, 351(6322), 137.
795
796 Armijo, R., Meyer, B. G. C. P., King, G. C. P., Rigo, A., & Papanastassiou, D. (1996).
797 Quaternary evolution of the Corinth Rift and its implications for the Late Cenozoic evolution
798 of the Aegean. *Geophysical Journal International*, *126*(1), 11-53.

799 Bell, R. E., McNeill, L. C., Bull, J. M., Henstock, T. J., Collier, R. L., & Leeder, M. R. (2009). Fault
800 architecture, basin structure and evolution of the Gulf of Corinth Rift, central Greece. *Basin
801 Research*, *21*(6), 824-855.

802 Binnie, A., Dunai, T. J., Binnie, S. A., Victor, P., González, G., & Bolten, A. (2016). Accelerated
803 late quaternary uplift revealed by 10Be exposure dating of marine terraces, Mejillones
804 Peninsula, northern Chile. *Quaternary Geochronology*, *36*, 12-27.

805 Boncio, P., Lavecchia, G., & Pace, B. (2004). Defining a model of 3D seismogenic sources for
806 Seismic Hazard Assessment applications: the case of central Apennines (Italy). *Journal of
807 Seismology*, *8*(3), 407-425.

808 Bornovas, J., Gaitanakis, P., & Spiridopoulos, A. (1984). *Geological map of Greece, 1:50,000,
809 Perachora Sheet.* Athens: IGME.

810 Boulton, S. J., & Stewart, I. S. (2015). Holocene coastal notches in the Mediterranean region:
811 Indicators of palaeoseismic clustering?. *Geomorphology*, *237*, 29-37.

812 Briole, P., Rigo, A., Lyon-Caen, H., Ruegg, J. C., Papazissi, K., Mitsakaki, C., ... & Deschamps,
813 A. (2000). Active deformation of the Corinth rift, Greece: results from repeated Global
814 Positioning System surveys between 1990 and 1995. *Journal of Geophysical Research: Solid
815 Earth*, *105*(B11), 25605-25625.

816 Burnside, 2010. Unpublished Thesis. University of Glasgow.

817 Cartwright, J. A., & Mansfield, C. S. (1998). Lateral displacement variation and lateral tip
818 geometry of normal faults in the Canyonlands National Park, Utah. *Journal of Structural
819 Geology*, *20*(1), 3-19.

820 Charalampakis, M., Lykousis, V., Sakellariou, D., Papatheodorou, G., & Ferentinos, G. (2014).
821 The tectono-sedimentary evolution of the Lechaion Gulf, the south eastern branch of the
822 Corinth graben, Greece. *Marine Geology*, *351*, 58-75.

823 Cheng, H., Edwards, R. L., Shen, C. C., Polyak, V. J., Asmerom, Y., Woodhead, J., ... & Wang,
824 X. (2013). Improvements in 230Th dating, 230Th and 234U half-life values, and U–Th

825   isotopic measurements by multi-collector inductively coupled plasma mass spectrometry.
826   *Earth and Planetary Science Letters*, 371, 82-91.

827   Clarke, P. J., Davies, R. R., England, P. C., Parsons, B., Billiris, H., Paradissis, D., ... & Bingley, R.
828   (1998). Crustal strain in central Greece from repeated GPS measurements in the interval
829   1989–1997. *Geophysical Journal International*, *135*(1), 195-214.

830   Collier, R. L., Leeder, M. R., Rowe, P. J., & Atkinson, T. C. (1992). Rates of tectonic uplift in
831   the Corinth and Megara basins, central Greece. *Tectonics*, *11*(6), 1159-1167.

832   Collier, R. E., Leeder, M. R., Trout, M., Ferentinos, G., Lyberis, E., & Papatheodorou, G.
833   (2000). High sediment yields and cool, wet winters: Test of last glacial paleoclimates in the
834   northern Mediterranean. *Geology*, *28*(11), 999-1002.

835   Collier, R. E., Pantosti, D., D'addezio, G., De Martini, P. M., Masana, E., & Sakellariou, D.
836   (1998). Paleoseismicity of the 1981 Corinth earthquake fault: Seismic contribution to
837   extensional strain in central Greece and implications for seismic hazard. *Journal of
838   Geophysical Research: Solid Earth*, *103*(B12), 30001-30019.

839   Cooper, F. J., Roberts, G. P., & Underwood, C. J. (2007). A comparison of 103–105 year uplift
840   rates on the South Alkyonides Fault, central Greece: Holocene climate stability and the
841   formation of coastal notches. *Geophysical Research Letters*, *34*(14).

842   Cowie, P. A., & Roberts, G. P. (2001). Constraining slip rates and spacings for active normal
843   faults. *Journal of Structural Geology*, *23*(12), 1901-1915.

844   Cowie, P. A., & Shipton, Z. K. (1998). Fault tip displacement gradients and process zone
845   dimensions. *Journal of Structural Geology*, *20*(8), 983-997.

846   Crémière, A., Lepland, A., Chand, S., Sahy, D., Condon, D. J., Noble, S. R., ... & Brunstad, H.
847   (2016). Timescales of methane seepage on the Norwegian margin following collapse of the
848   Scandinavian Ice Sheet. *Nature communications*, 7, 11509.

849   Crone, A. J., & Haller, K. M. (1991). Segmentation and the coseismic behavior of Basin and
850   Range normal faults: examples from east-central Idaho and southwestern Montana, USA.
851   *Journal of Structural Geology*, 13(2), 151-164.

852   Davies, R., England, P. C., Parsons, B., Billiris, H., Paradissis, D., & Veis, G. (1997). Geodetic
853   strain of Greece in the interval 1892–1992. *Journal of Geophysical Research: Solid Earth*,
854   *102*(B11), 24571-24588.

855   DePolo, C. M., Clark, D. G., Slemmons, D. B., & Ramelli, A. R. (1991). Historical surface
856   faulting in the Basin and Range province, western North America: implications for fault
857   segmentation. *Journal of structural Geology*, *13*(2), 123-136.

858 Devescovi, M., & Iveša, L. (2008). Colonization patterns of the date mussel Lithophaga
859 lithophaga (L., 1758) on limestone breakwater boulders of a marina. *Periodicum biologorum*,
860 *110*(4), 339-345.

861 Dia, A. N., Cohen, A. S., O'nions, R. K., & Jackson, J. A. (1997). Rates of uplift investigated
862 through 230Th dating in the Gulf of Corinth (Greece). *Chemical Geology*, *138*(3-4), 171-184.

863 Dunai, T. (2010). *Cosmogenic nuclides, principles, concepts and applications in the Earth*
864 *surface sciences.* Cambridge: Cambridge University Press

865 Dutton, A., Carlson, A. E., Long, A., Milne, G. A., Clark, P. U., DeConto, R., ... & Raymo, M. E.
866 (2015). Sea-level rise due to polar ice-sheet mass loss during past warm periods. *science*,
867 *349*(6244), aaa4019.

868 Dutton, A., & Lambeck, K. (2012). Ice volume and sea level during the last interglacial.
869 *science*, *337*(6091), 216-219.

870 Faure Walker, J. P., Visini, F., Roberts, G., Galasso, C., McCaffrey, K., & Mildon, Z. (2018).
871 Variable Fault Geometry Suggests Detailed Fault-Slip-Rate Profiles and Geometries Are
872 Needed for Fault-Based Probabilistic Seismic Hazard Assessment (PSHA). *Bulletin of the*
873 *Seismological Society of America*, *109*(1), 110-123.

874 Fernández-Blanco, D., de Gelder, G., Lacassin, R., & Armijo, R. (2019). A new crustal fault
875 formed the modern Corinth Rift. *Earth-Science Reviews*, 102919.

876 Ferrill, D. A., & Morris, A. P. (2001). Displacement gradient and deformation in normal fault
877 systems. *Journal of Structural Geology*, *23*(4), 619-638.

878 Field, E. H., Arrowsmith, R. J., Biasi, G. P., Bird, P., Dawson, T. E., Felzer, K. R., ... & Michael,
879 A. J. (2014). Uniform California earthquake rupture forecast, version 3 (UCERF3)—The time-
880 independent model. *Bulletin of the Seismological Society of America*, *104*(3), 1122-1180.

881 Field, E. H., Milner, K. R., Hardebeck, J. L., Page, M. T., van der Elst, N., Jordan, T. H., ... &
882 Werner, M. J. (2017). A spatiotemporal clustering model for the third Uniform California
883 Earthquake Rupture Forecast (UCERF3-ETAS): Toward an operational earthquake forecast.
884 *Bulletin of the Seismological Society of America*, *107*(3), 1049-1081.

885 Fossen, H., & Rotevatn, A. (2016). Fault linkage and relay structures in extensional settings—
886 A review. *Earth-Science Reviews*, *154*, 14-28.

887 Gallen, S. F., Wegmann, K. W., Bohnenstiehl, D. R., Pazzaglia, F. J., Brandon, M. T., &
888 Fassoulas, C. (2014). Active simultaneous uplift and margin-normal extension in a forearc
889 high, Crete, Greece. *Earth and Planetary Science Letters*, *398*, 11-24.

890 Galli, P., Galadini, F., & Pantosti, D. (2008). Twenty years of paleoseismology in Italy. *Earth-*
891 *Science Reviews*, *88*(1-2), 89-117.

892   Gallup, C. D., Cheng, H., Taylor, F. W., & Edwards, R. L. (2002). Direct determination of the
893   timing of sea level change during Termination II. *Science*, *295*(5553), 310-313.

894   Grant, K. M., Rohling, E. J., Ramsey, C. B., Cheng, H., Edwards, R. L., Florindo, F., ... &
895   Williams, F. (2014). Sea-level variability over five glacial cycles. *Nature communications*, 5,
896   5076.

897   Griggs, G. B., Trenhaile, A. S., Carter, R. W. G., & Woodroffe, C. D. (1994). *Coastal cliffs and*
898   *platforms* (pp. 425-450). Cambridge University Press, Cambridge, UK.

899   Gupta, A., & Scholz, C. H. (2000). A model of normal fault interaction based on observations
900   and theory. *Journal of Structural Geology*, *22*(7), 865-879.

901   Hearty, P. J., Hollin, J. T., Neumann, A. C., O'Leary, M. J., & McCulloch, M. (2007). Global sea-
902   level fluctuations during the Last Interglaciation (MIS 5e). *Quaternary Science Reviews*,
903   *26*(17-18), 2090-2112.

904   Houghton, 2010. Unpublished Thesis. Birkbeck College, University of London.

905   Hubert, A., King, G., Armijo, R., Meyer, B., & Papanastasiou, D. (1996). Fault re-activation,
906   stress interaction and rupture propagation of the 1981 Corinth earthquake sequence. *Earth*
907   *and Planetary Science Letters*, *142*(3-4), 573-585.

908   Huggins, P., Watterson, J., Walsh, J. J., & Childs, C. (1995). Relay zone geometry and
909   displacement transfer between normal faults recorded in coal-mine plans. *Journal of*
910   *Structural Geology*, *17*(12), 1741-1755.

911   Iezzi, F., Mildon, Z., Walker, J. F., Roberts, G., Goodall, H., Wilkinson, M., & Robertson, J.
912   (2018). Coseismic throw variation across along-strike bends on active normal faults:
913   Implications for displacement versus length scaling of earthquake ruptures. *Journal of*
914   *Geophysical Research: Solid Earth*, *123*(11), 9817-9841.

915   Iezzi, F., Roberts, G., Walker, J. F., & Papanikolaou, I. (2019). Occurrence of partial and total
916   coseismic ruptures of segmented normal fault systems: Insights from the Central Apennines,
917   Italy. *Journal of Structural Geology*, *126*, 83-99.

918   Jackson, J. A., Gagnepain, J., Houseman, G., King, G. C. P., Papadimitriou, P., Soufleris, C., &
919   Virieux, J. (1982). Seismicity, normal faulting, and the geomorphological development of the
920   Gulf of Corinth (Greece): the Corinth earthquakes of February and March 1981. *Earth and*
921   *Planetary Science Letters*, *57*(2), 377-397.

922   Jara-Muñoz, J., Melnick, D., Zambrano, P., Rietbrock, A., González, J., Argandoña, B., &
923   Strecker, M. R. (2017). Quantifying offshore fore-arc deformation and splay-fault slip using
924   drowned Pleistocene shorelines, Arauco Bay, Chile. *Journal of Geophysical Research: Solid*
925   *Earth*, *122*(6), 4529-4558.

926 Kershaw, S., & Guo, L. (2001). Marine notches in coastal cliffs: indicators of relative sea-level
927 change, Perachora Peninsula, central Greece. *Marine Geology*, *179*(3-4), 213-228.

928 Kershaw, S., & Guo, L. (2003). Pleistocene cyanobacterial mounds in the Perachora
929 Peninsula, Gulf of Corinth, Greece: structure and applications to interpreting sea-level
930 history and terrace sequences in an unstable tectonic setting. *Palaeogeography,*
931 *Palaeoclimatology, Palaeoecology*, *193*(3-4), 503-514.

932 Kershaw, S., & Guo, L. (2006). Pleistocene calcified cyanobacterial mounds, Perachora
933 Peninsula, central Greece: a controversy of growth and history. *Geological Society, London,*
934 *Special Publications*, *255*(1), 53-69.

935 King, G. C., Stein, R. S., & Lin, J. (1994). Static stress changes and the triggering of
936 earthquakes. *Bulletin of the Seismological Society of America*, *84*(3), 935-953.

937 Kopp, R. E., Simons, F. J., Mitrovica, J. X., Maloof, A. C., & Oppenheimer, M. (2009).
938 Probabilistic assessment of sea level during the last interglacial stage. *Nature*, *462*(7275),
939 863.

940 Lajoie, K. R. (1986). Coastal tectonics. Active tectonics, 95-124.

941 Lambeck, K., Esat, T. M., & Potter, E. K. (2002). Links between climate and sea levels for the
942 past three million years. *Nature*, 419(6903), 199.

943 Leeder, M. R., McNeill, L. C., Ll Collier, R. E., Portman, C., Rowe, P. J., Andrews, J. E., &
944 Gawthorpe, R. L. (2003). Corinth rift margin uplift: New evidence from Late Quaternary
945 marine shorelines. *Geophysical Research Letters*, *30*(12).

946 Leeder, M. R., Portman, C., Andrews, J. E., Collier, R. L., Finch, E., Gawthorpe, R. L., ... &
947 Rowe, P. (2005). Normal faulting and crustal deformation, Alkyonides Gulf and Perachora
948 peninsula, eastern Gulf of Corinth rift, Greece. *Journal of the Geological Society*, *162*(3), 549-
949 561.

950 Leeder, M. R., Seger, M. J., & Stark, C. P. (1991). Sedimentation and tectonic geomorphology
951 adjacent to major active and inactive normal faults, southern Greece. *Journal of the*
952 *Geological Society*, *148*(2), 331-343.

953 Licciardi, J. M., Denoncourt, C. L., & Finkel, R. C. (2008). Cosmogenic 36Cl production rates
954 from Ca spallation in Iceland. *Earth and Planetary Science Letters*, *267*(1-2), 365-377.

955 Machette, M. N., Personius, S. F., Nelson, A. R., Schwartz, D. P., & Lund, W. R. (1991). The
956 Wasatch fault zone, Utah—Segmentation and history of Holocene earthquakes. *Journal of*
957 *Structural Geology*, *13*(2), 137-149.

958 Marrero, S. M., Phillips, F. M., Caffee, M. W., & Gosse, J. C. (2016). CRONUS-Earth
959 cosmogenic 36Cl calibration. *Quaternary Geochronology*, *31*, 199-219.

960   McGrath, A. G., & Davison, I. (1995). Damage zone geometry around fault tips. *Journal of*
961   *Structural Geology*, *17*(7), 1011-1024.

962   McLeod, A. E., Dawers, N. H., & Underhill, J. R. (2000). The propagation and linkage of
963   normal faults: insights from the Strathspey–Brent–Statfjord fault array, northern North Sea.
964   *Basin Research*, *12*(3-4), 263-284.

965   McNeill, L. C., & Collier, R. L. (2004). Uplift and slip rates of the eastern Eliki fault segment,
966   Gulf of Corinth, Greece, inferred from Holocene and Pleistocene terraces. *Journal of the*
967   *Geological Society*, *161*(1), 81-92.

968   McNeill, L. C., Cotterill, C. J., Henstock, T. J., Bull, J. M., Stefatos, A., Collier, R. L., ... & Hicks,
969   S. E. (2005). Active faulting within the offshore western Gulf of Corinth, Greece: Implications
970   for models of continental rift deformation. *Geology*, *33*(4), 241-244.

971   Mechernich, S., Schneiderwind, S., Mason, J., Papanikolaou, I. D., Deligiannakis, G.,
972   Pallikarakis, A., ... & Reicherter, K. (2018). The seismic history of the Pisia fault (eastern
973   Corinth rift, Greece) from fault plane weathering features and cosmogenic 36Cl dating.
974   *Journal of Geophysical Research: Solid Earth*, *123*(5), 4266-4284.

975   Meschis, M., Roberts, G. P., Robertson, J., & Briant, R. M. (2018). The Relationships Between
976   Regional Quaternary Uplift, Deformation Across Active Normal Faults, and Historical
977   Seismicity in the Upper Plate of Subduction Zones: The Capo D'Orlando Fault, NE Sicily.
978   *Tectonics*, *37*(5), 1231-1255.

979   Meschis, M., Roberts, G. P., Mildon, Z. K., Robertson, J., Michetti, A. M., & Walker, J. F.
980   (2019). Slip on a mapped normal fault for the 28 th December 1908 Messina earthquake
981   (Mw 7.1) in Italy. *Scientific reports*, 9(1), 1-8.

982   Mildon, Z. K., Toda, S., Faure Walker, J. P., & Roberts, G. P. (2016a). Evaluating models of
983   Coulomb stress transfer: Is variable fault geometry important?. *Geophysical Research*
984   *Letters*, *43*(24).

985   Miller, W. R., & Mason, T. R. (1994). Erosional features of coastal beachrock and aeolianite
986   outcrops in Natal and Zululand, South Africa. *Journal of Coastal Research*, 374-394.

987   Moretti, I., Sakellariou, D., Lykousis, V., & Micarelli, L. (2003). The Gulf of Corinth: an active
988   half graben?. *Journal of Geodynamics*, *36*(1-2), 323-340.

989   Morewood, N. C., & Roberts, G. P. (1997). Geometry, kinematics and rates of deformation in
990   a normal fault segment boundary, central Greece. *Geophysical Research Letters*, *24*(23),
991   3081-3084.

992   Morewood, N. C., & Roberts, G. P. (1999). Lateral propagation of the surface trace of the
993   South Alkyonides normal fault segment, central Greece: its impact on models of fault
994   growth and displacement–length relationships. *Journal of Structural Geology*, *21*(6), 635-
995   652.

996 Morewood, N. C., & Roberts, G. P. (2001). Comparison of surface slip and focal mechanism
997 slip data along normal faults: an example from the eastern Gulf of Corinth, Greece. *Journal*
998 *of Structural Geology*, *23*(2-3), 473-487.

999 Morewood, N. C., & Roberts, G. P. (2002). Surface observations of active normal fault
1000 propagation: implications for growth. *Journal of the Geological Society*, *159*(3), 263-272.

1001 Mozafari, N., SÜMER, Ö., Tikhomirov, D., Ivy-Ochs, S., Alfimov, V., Vockenhuber, C., ... &
1002 Akcar, N. (2019). Holocene seismic activity of the Priene-Sazlı Fault revealed by cosmogenic
1003 36 Cl, Western Anatolia, Turkey 2. *Turkish Journal of Earth Sciences*, 28(3).

1004 Muhs, D. R., & Szabo, B. J. (1994). New uranium-series ages of the Waimanalo Limestone,
1005 Oahu, Hawaii: implications for sea level during the last interglacial period. *Marine Geology*,
1006 *118*(3-4), 315-326.

1007 Nixon, C. W., McNeill, L. C., Bull, J. M., Bell, R. E., Gawthorpe, R. L., Henstock, T. J., ... &
1008 Ferentinos, G. (2016). Rapid spatiotemporal variations in rift structure during development
1009 of the Corinth Rift, central Greece. *Tectonics*, *35*(5), 1225-1248.

1010 O'Leary, M. J., Hearty, P. J., Thompson, W. G., Raymo, M. E., Mitrovica, J. X., & Webster, J.
1011 M. (2013). Ice sheet collapse following a prolonged period of stable sea level during the last
1012 interglacial. *Nature Geoscience*, *6*(9), 796.

1013 Pace, B., Peruzza, L., Lavecchia, G., & Boncio, P. (2006). Layered seismogenic source model
1014 and probabilistic seismic-hazard analyses in central Italy. *Bulletin of the Seismological*
1015 *Society of America*, *96*(1), 107-132.

1016 Pace, B., Peruzza, L., & Visini, F. (2010). LASSCI2009. 2: layered earthquake rupture forecast
1017 model for central Italy, submitted to the CSEP project. *Annals of Geophysics*.

1018 Pace, B., Visini, F., & Peruzza, L. (2016). FiSH: MATLAB tools to turn fault data into seismic-
1019 hazard models. *Seismological Research Letters*, 87(2A), 374-386.

1020 Papanikolaou, I. D., & Roberts, G. P. (2007). Geometry, kinematics and deformation rates
1021 along the active normal fault system in the southern Apennines: Implications for fault
1022 growth. *Journal of Structural Geology*, *29*(1), 166-188.

1023 Papanikolaou, I. D., Roberts, G. P., & Michetti, A. M. (2005). Fault scarps and deformation
1024 rates in Lazio–Abruzzo, Central Italy: Comparison between geological fault slip-rate and GPS
1025 data. *Tectonophysics*, *408*(1-4), 147-176.

1026 Peacock, D. C. P. (2002). Propagation, interaction and linkage in normal fault systems. *Earth-*
1027 *Science Reviews*, *58*(1-2), 121-142.

1028 Peacock, D. C. P., & Sanderson, D. J. (1991). Displacements, segment linkage and relay
1029 ramps in normal fault zones. *Journal of Structural Geology*, *13*(6), 721-733.

1030 Peacock, D. C. P., & Sanderson, D. J. (1994). Geometry and development of relay ramps in
1031 normal fault systems. *AAPG bulletin*, *78*(2), 147-165.

1032 Peharda, M., Puljas, S., Chauvaud, L., Schöne, B. R., Ezgeta-Balić, D., & Thébault, J. (2015).
1033 Growth and longevity of Lithophaga lithophaga: what can we learn from shell structure and
1034 stable isotope composition?. *Marine biology*, 162(8), 1531-1540.

1035 Perrin, C., Manighetti, I., & Gaudemer, Y. (2016). Off-fault tip splay networks: A genetic and
1036 generic property of faults indicative of their long-term propagation. *Comptes Rendus*
1037 *Geoscience*, *348*(1), 52-60.

1038 Pirazzoli, P. A. (1986). Marine notches. In *Sea-Level Research* (pp. 361-400). Springer,
1039 Dordrecht.

1040 Pirazzoli, P. A., Stiros, S. C., Arnold, M., Laborel, J., Laborel-Deguen, F., & Papageorgiou, S.
1041 (1994). Episodic uplift deduced from Holocene shorelines in the Perachora Peninsula,
1042 Corinth area, Greece. *Tectonophysics*, *229*(3-4), 201-209.

1043 Portman, C., Andrews, J. E., Rowe, P. J., Leeder, M. R., & Hoogewerff, J. (2005). Submarine-
1044 spring controlled calcification and growth of large Rivularia bioherms, Late Pleistocene (MIS
1045 5e), Gulf of Corinth, Greece. *Sedimentology*, *52*(3), 441-465.

1046 Richter, D. K., & Sedat, R. (1983). Brackish-water oncoids composed of blue-green and red
1047 algae from a Pleistocene terrace near Corinth, Greece. In *Coated grains* (pp. 299-307).
1048 Springer, Berlin, Heidelberg.

1049 Roberts, G. P. (1996a). Noncharacteristic normal faulting surface ruptures from the Gulf of
1050 Corinth, Greece. *Journal of Geophysical Research: Solid Earth*, *101*(B11), 25255-25267.

1051 Roberts, G. P. (1996b). Variation in fault-slip directions along active and segmented normal
1052 fault systems. *Journal of Structural Geology*, 18(6), 835-845.

1053 Roberts, G. P., & Koukouvelas, I. (1996). Structural and seismological segmentation of the
1054 Gulf of Corinth fault system: implications for models of fault growth.

1055 Roberts, G. P., Houghton, S. L., Underwood, C., Papanikolaou, I., Cowie, P. A., van Calsteren,
1056 P., ... & McArthur, J. M. (2009). Localization of Quaternary slip rates in an active rift in 105
1057 years: An example from central Greece constrained by 234U-230Th coral dates from uplifted
1058 paleoshorelines. *Journal of Geophysical Research: Solid Earth*, *114*(B10).

1059 Roberts, G. P., Meschis, M., Houghton, S., Underwood, C., & Briant, R. M. (2013). The
1060 implications of revised Quaternary palaeoshoreline chronologies for the rates of active
1061 extension and uplift in the upper plate of subduction zones. *Quaternary Science Reviews*, *78*,
1062 169-187.

1063 Roberts, G. P., & Michetti, A. M. (2004). Spatial and temporal variations in growth rates
1064 along active normal fault systems: an example from The Lazio–Abruzzo Apennines, central
1065 Italy. *Journal of Structural Geology*, *26*(2), 339-376.

1066 Roberts, S., & Jackson, J. (1991). Active normal faulting in central Greece: an overview.
1067 *Geological Society, London, Special Publications*, *56*(1), 125-142.

1068 Robertson, J., Meschis, M., Roberts, G. P., Ganas, A., & Gheorghiu, D. (2019). Temporally
1069 constant Quaternary uplift rates and their relationship with extensional upper-plate faults in
1070 south Crete (Greece), constrained with 36Cl cosmogenic exposure dating. *Tectonics*.

1071 Sachpazi, M., Clément, C., Laigle, M., Hirn, A., & Roussos, N. (2003). Rift structure, evolution,
1072 and earthquakes in the Gulf of Corinth, from reflection seismic images. *Earth and Planetary
1073 Science Letters*, *216*(3), 243-257.

1074 Sakellariou, D., Lykousis, V., Alexandri, S., Kaberi, H., Rousakis, G., Nomikou, P., ... & Ballas,
1075 D. (2007). Faulting, seismic-stratigraphic architecture and late quaternary evolution of the
1076 Gulf of Alkyonides Basin-East Gulf of Corinth, Central Greece. *Basin Research*, *19*(2), 273-
1077 295.

1078 Schimmelpfennig, I., Benedetti, L., Finkel, R., Pik, R., Blard, P. H., Bourles, D., ... & Williams,
1079 A. (2009). Sources of in-situ 36Cl in basaltic rocks. Implications for calibration of production
1080 rates. *Quaternary Geochronology*, *4*(6), 441-461.

1081 Schlagenhauf, A., Gaudemer, Y., Benedetti, L., Manighetti, I., Palumbo, L., Schimmelpfennig,
1082 I., ... & Pou, K. (2010). Using in situ Chlorine-36 cosmonuclide to recover past earthquake
1083 histories on limestone normal fault scarps: a reappraisal of methodology and
1084 interpretations. *Geophysical Journal International*, *182*(1), 36-72.

1085 Schlische, R. W., & Anders, M. H. (1996). Stratigraphic effects and tectonic implications of
1086 the growth of normal faults and extensional basins. *Special Papers-Geological Society of
1087 America*, 183-203.

1088 Schlische, R. W., Young, S. S., Ackermann, R. V., & Gupta, A. (1996). Geometry and scaling
1089 relations of a population of very small rift-related normal faults. *Geology*, *24*(8), 683-686.

1090 Schneiderwind, S., Boulton, S. J., Papanikolaou, I., Kázmér, M., & Reicherter, K. (2017a).
1091 Numerical modeling of tidal notch sequences on rocky coasts of the Mediterranean Basin.
1092 *Journal of Geophysical Research: Earth Surface*, 122(5), 1154-1181.

1093 Schneiderwind, S., Boulton, S. J., Papanikolaou, I., & Reicherter, K. (2017b). Innovative tidal
1094 notch detection using TLS and fuzzy logic: Implications for palaeo-shorelines from
1095 compressional (Crete) and extensional (Gulf of Corinth) tectonic settings. *Geomorphology*,
1096 *283*, 189-200.

1097 Scholz, C. H., & Gupta, A. (2000). Fault interactions and seismic hazard. *Journal of
1098 Geodynamics*, *29*(3-5), 459-467.

1099   Scholz, C. H., & Lawler, T. M. (2004). Slip tapers at the tips of faults and earthquake
1100   ruptures. *Geophysical research letters*, *31*(21).

1101   Scott, A (1995). Unpublished Thesis, University of Manchester

1102   Siddall, M., Rohling, E. J., Almogi-Labin, A., Hemleben, C., Meischner, D., Schmelzer, I., &
1103   Smeed, D. A. (2003). Sea-level fluctuations during the last glacial cycle. *Nature*, *423*(6942),
1104   853.

1105   Sieh, K., Stuiver, M., & Brillinger, D. (1989). A more precise chronology of earthquakes
1106   produced by the San Andreas fault in southern California. *Journal of Geophysical Research:*
1107   *Solid Earth*, 94(B1), 603-623.

1108   Spratt, R. M., & Lisiecki, L. E. (2016). A Late Pleistocene sea level stack. Climate of the Past,
1109   12(4), 1079-1092.
1110
1111   Stefatos, A., Papatheodorou, G., Ferentinos, G., Leeder, M., & Collier, R. (2002). Seismic
1112   reflection imaging of active offshore faults in the Gulf of Corinth: their seismotectonic
1113   significance. *Basin Research*, *14*(4), 487-502.

1114   Stirling, C. H., & Andersen, M. B. (2009). Uranium-series dating of fossil coral reefs:
1115   extending the sea-level record beyond the last glacial cycle. *Earth and Planetary Science*
1116   *Letters*, *284*(3-4), 269-283.

1117   Stirling, C. H., Esat, T. M., Lambeck, K., & McCulloch, M. T. (1998). Timing and duration of
1118   the Last Interglacial: evidence for a restricted interval of widespread coral reef growth.
1119   *Earth and Planetary Science Letters*, *160*(3-4), 745-762.

1120   Stiros, S. C., & Pirazzoli, P. A. (1995). Palaeoseismic studies in Greece: a review. *Quaternary*
1121   *International*, *25*, 57-63.

1122   Stone, J., Lambeck, K., Fifield, L. K., Evans, J. T., & Cresswell, R. G. (1996). A lateglacial age for
1123   the main rock platform, western Scotland. *Geology*, *24*(8), 707-710.

1124   Stuart, F. M., & Dunai, T. J. (2009). Advances in cosmogenic isotope research from CRONUS-
1125   EU. *Quaternary Geochronology*, 4(6), 435-436.

1126   Taylor, B., Weiss, J. R., Goodliffe, A. M., Sachpazi, M., Laigle, M., & Hirn, A. (2011). The
1127   structures, stratigraphy and evolution of the Gulf of Corinth rift, Greece. *Geophysical Journal*
1128   *International*, *185*(3), 1189-1219.

1129   Taymaz, T., Jackson, J., & McKenzie, D. (1991). Active tectonics of the north and central
1130   Aegean Sea. *Geophysical Journal International*, *106*(2), 433-490.

1131   Toda, S., Stein, R. S., Richards-Dinger, K., & Bozkurt, S. B. (2005). Forecasting the evolution of
1132   seismicity in southern California: Animations built on earthquake stress transfer. *Journal of*
1133   *Geophysical Research: Solid Earth*, *110*(B5).

1134   Valentini, A., Visini, F., & Pace, B. (2017). Integrating faults and past earthquakes into a
1135   probabilistic seismic hazard model for peninsular Italy. *Natural Hazards Earth System*
1136   *Sciences*.

1137   Vita-Finzi, C. (1993). Evaluating late Quaternary uplift in Greece and Cyprus. *Geological*
1138   *Society, London, Special Publications*, *76*(1), 417-424.

1139   Waelbroeck, C., Labeyrie, L., Michel, E., Duplessy, J. C., McManus, J. F., Lambeck, K., ... &
1140   Labracherie, M. (2002). Sea-level and deep water temperature changes derived from
1141   benthic foraminifera isotopic records. *Quaternary Science Reviews*, 21(1-3), 295-305.

1142   Wells, D. L., & Coppersmith, K. J. (1994). New empirical relationships among magnitude,
1143   rupture length, rupture width, rupture area, and surface displacement. *Bulletin of the*
1144   *seismological Society of America*, *84*(4), 974-1002.

1145   Wesnousky, S. G. (2008). Displacement and geometrical characteristics of earthquake
1146   surface ruptures: Issues and implications for seismic-hazard analysis and the process of
1147   earthquake rupture. *Bulletin of the Seismological Society of America*, *98*(4), 1609-1632.

1148   Wesnousky, S. G., & Biasi, G. P. (2011). The length to which an earthquake will go to rupture.
1149   *Bulletin of the Seismological Society of America*, *101*(4), 1948-1950.

1150   Westaway, R. (1993). Quaternary uplift of southern Italy. *Journal of Geophysical Research:*
1151   *Solid Earth*, *98*(B12), 21741-21772.

1152   Wu, D., & Bruhn, R. L. (1994). Geometry and kinematics of active normal faults, South
1153   Oquirrh Mountains, Utah: implication for fault growth. Journal of Structural Geology, 16(8),
1154   1061-1075.

1155   Willemse, E. J., Pollard, D. D., & Aydin, A. (1996). Three-dimensional analyses of slip
1156   distributions on normal fault arrays with consequences for fault scaling. *Journal of Structural*
1157   *Geology*, *18*(2-3), 295-309.

1158   Yielding, G., Needham, T., & Jones, H. (1996). Sampling of fault populations using sub-
1159   surface data: a review. *Journal of Structural Geology*, 18(2-3), 135-146.

1160   Zhang, P., Slemmons, D. B., & Mao, F. (1991). Geometric pattern, rupture termination and
1161   fault segmentation of the Dixie Valley—Pleasant Valley active normal fault system, Nevada,
1162   USA. *Journal of Structural Geology*, 13(2), 165-176.

1163   Figures
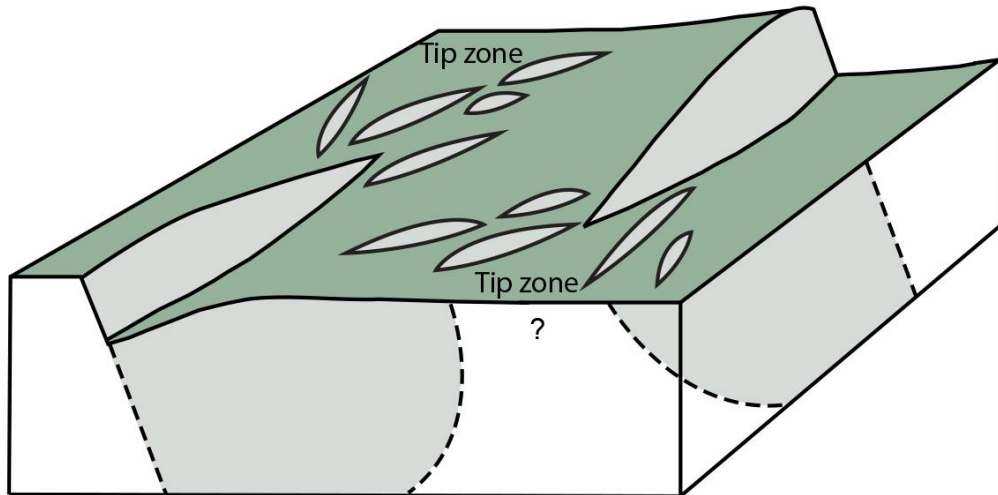
1164

Figure 1: Schematic diagram of a possible tip zone deformation where the tips of two along-strike faults overlap.

1165
1166
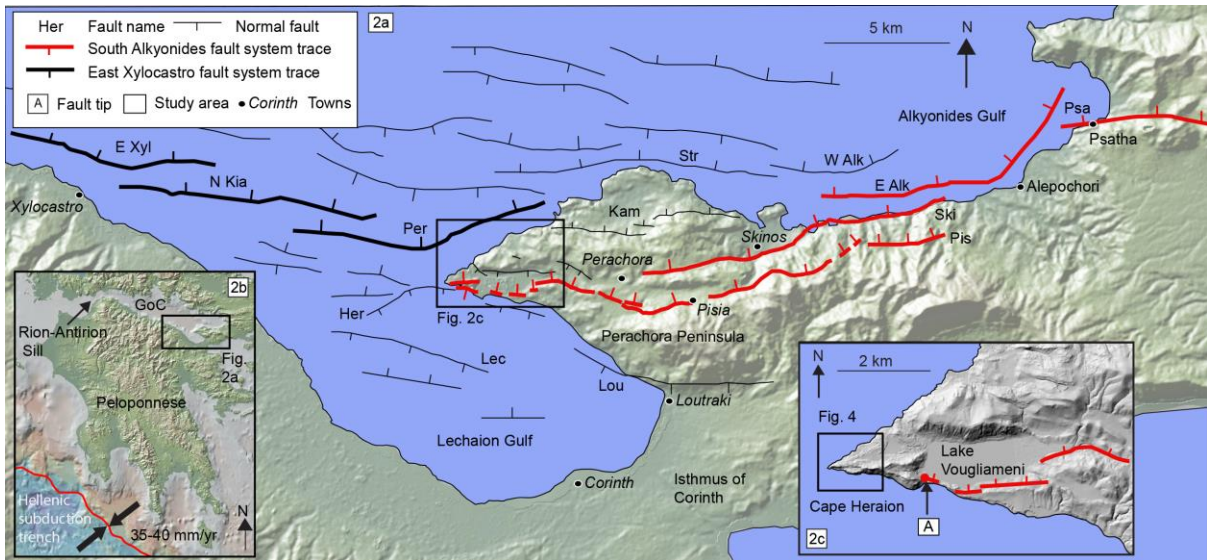
1167

Figure 2: (a) Map of the eastern Gulf of Corinth and the Perachora Peninsula, surface trace of the South Alkyonides Fault system (SAFS) (red) (Morewood and Roberts, 2002), East Xylocastro Fault System (EXFS) trace (Bold) as per Nixon et al., 2016, all other faults as per Nixon et al., 2016. (b) Location of the Gulf of Corinth and Hellenic subduction trench taken from Kreemer and Chamot-Rooke (2004), GPS data from Nocquet (2012). (c) 5 m Digital Elevation Model showing the western surface trace of the SAFS as per Morewood and Roberts (2002) and Cape Heraion. 'A' marks the location of the 'on-fault' tip of the SAFS (Morewood and Roberts, 1999).

1168
1169
1170
1171
1172
1173
1174
1175
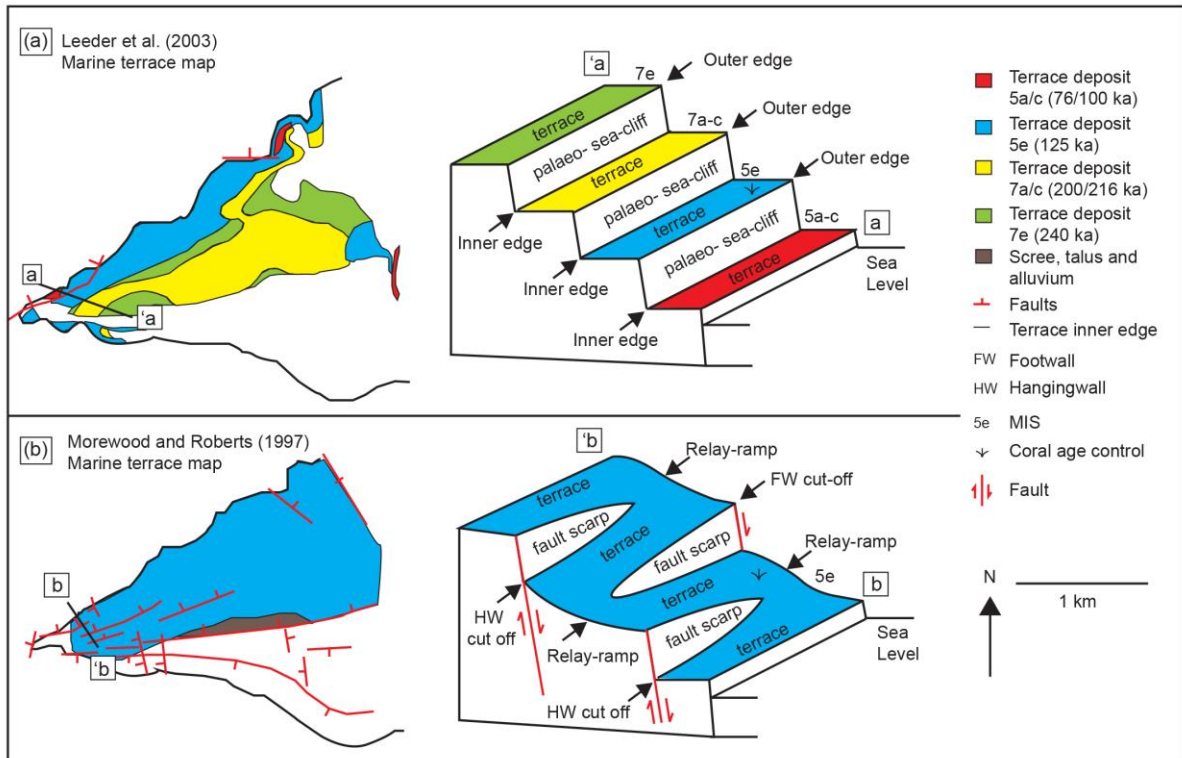
1176

Figure 3: Comparison of two explanations for the observed geomorphology on Cape
Heraion. (a) Geological map redrawn from Leeder et al. (2003) and interpreted schematic 3D
diagram, Leeder et al. (2003) suggest a sequence of palaeoshorelines from MIS 5a/c (76.5
ka/100 ka) to 7e (240 ka). (b) Geological map redrawn from Morewood and Roberts (1997)
and interpreted schematic 3D diagram, Morewood and Roberts (1997) suggest Cape
Heraion is linked to the MIS 5e 125 ka highstand and has been latterly faulted.
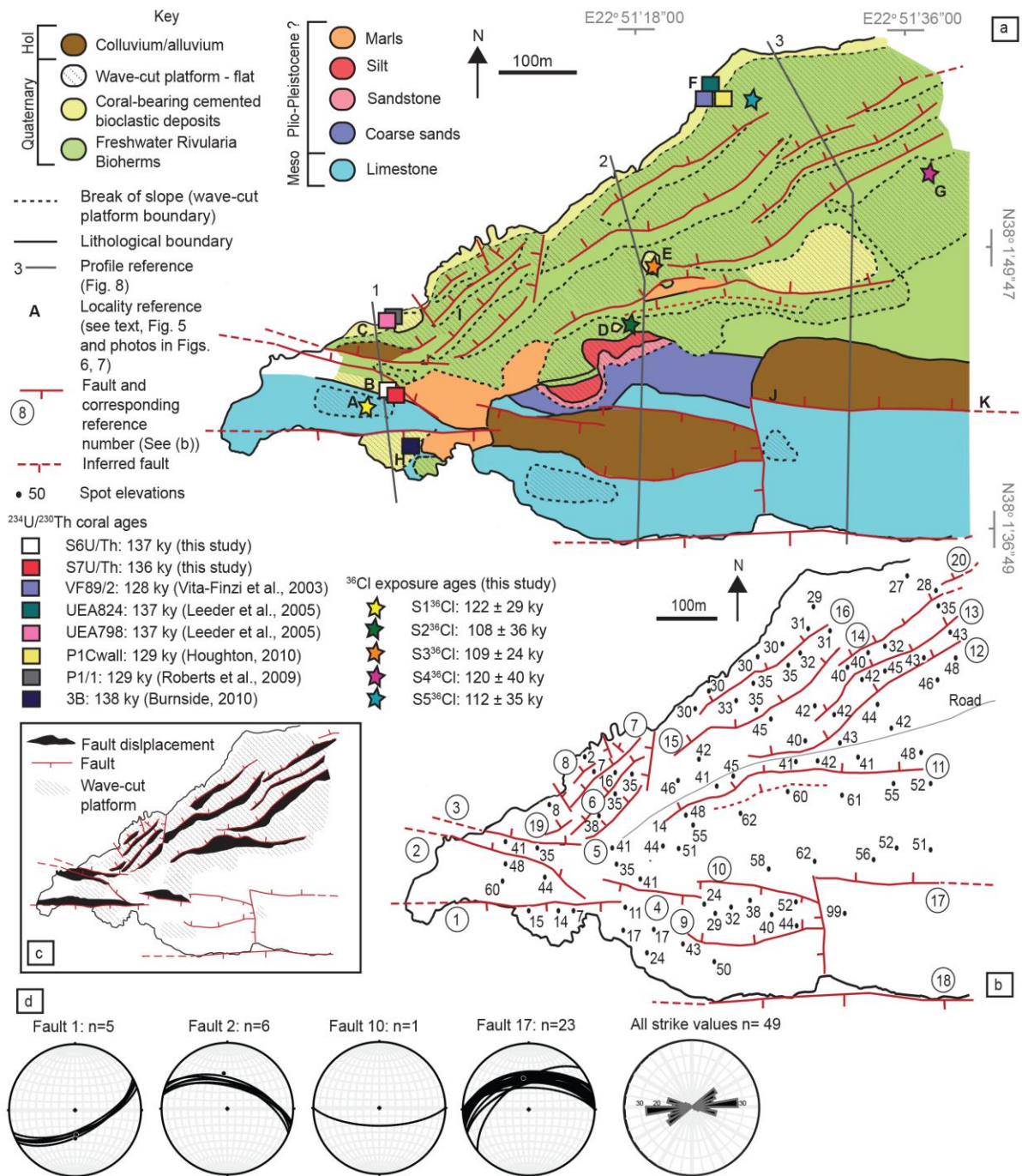
1183

Figure 4: (a) Geological and geomorphological map of Cape Heraion, age controls from this
study and other coral studies (Vita-Finzi et al., 2003; Leeder et al., 2005; Roberts et al., 2009;
Burnside, 2010; Houghton, 2010). (b) Fault map of Cape Heraion and spot height elevations
used to plot the fault displacement in (c). (d) Stereonet plots for faults 1, 2, 10 and 17, rose
diagram representing all measured strike values.

(a) Stratigraphic and structural relationships at dated localities from west to east at Cape Heraion

(b) Stratigraphic logs at the time when the wave-cut platform formed
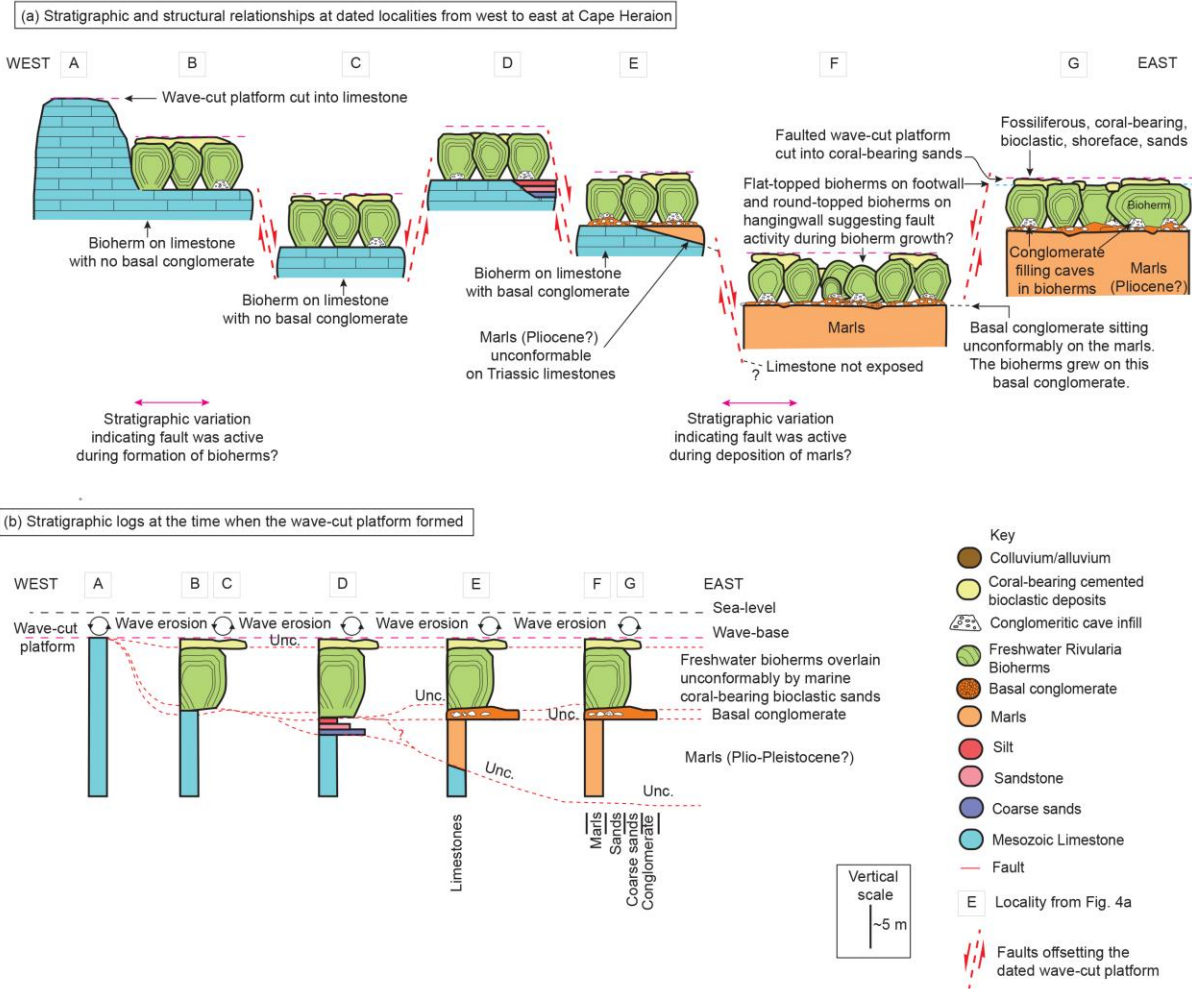
1189

Figure 5: (a) Stratigraphic and structural relationships and (b) stratigraphic logs for dated localities from West to East, see Figure 4 for localities
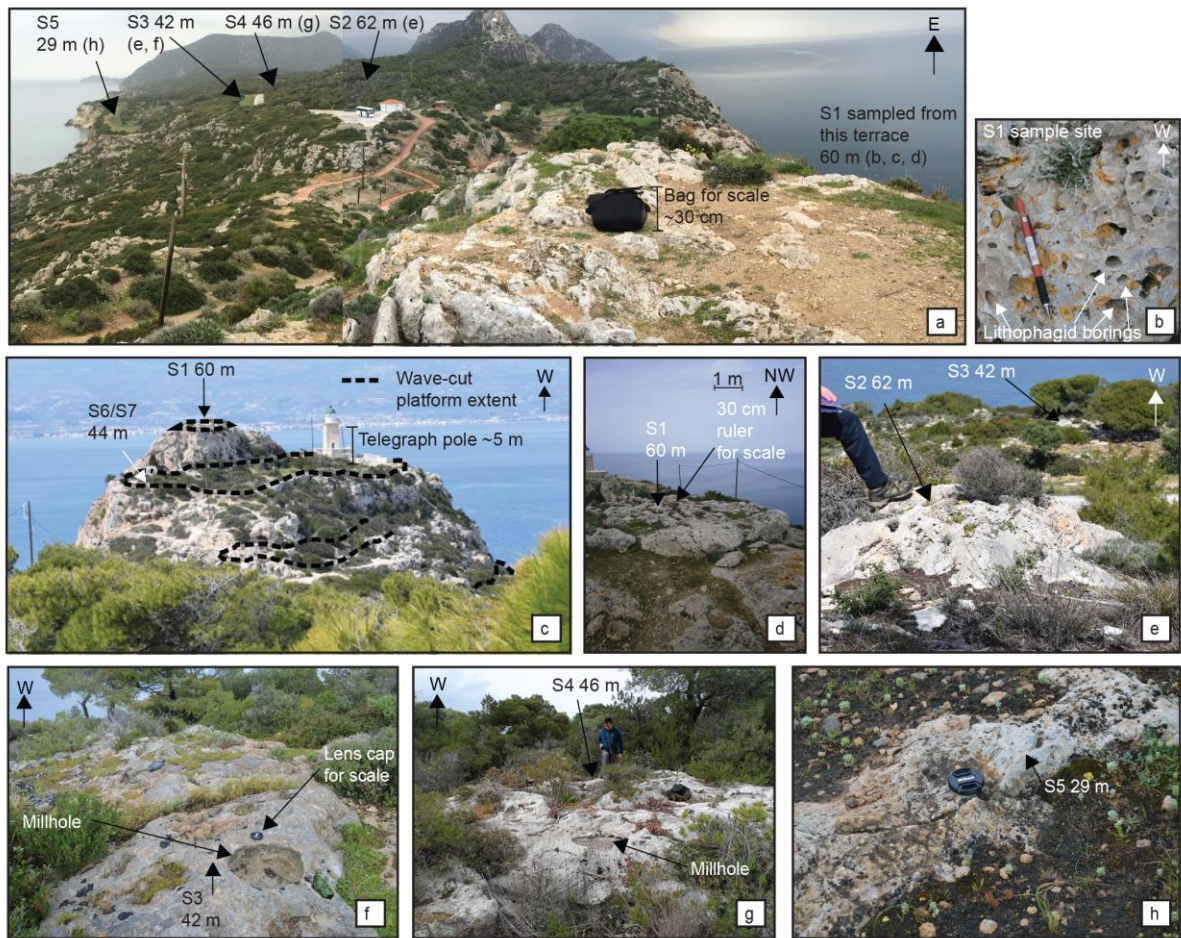
1192

Figure 6: (a) overview of ^{36}Cl sample locations. (b-h) Photographs of ^{36}Cl and ^{234}U/^{230}Th sample locations. See Figure 4a for locations of samples.
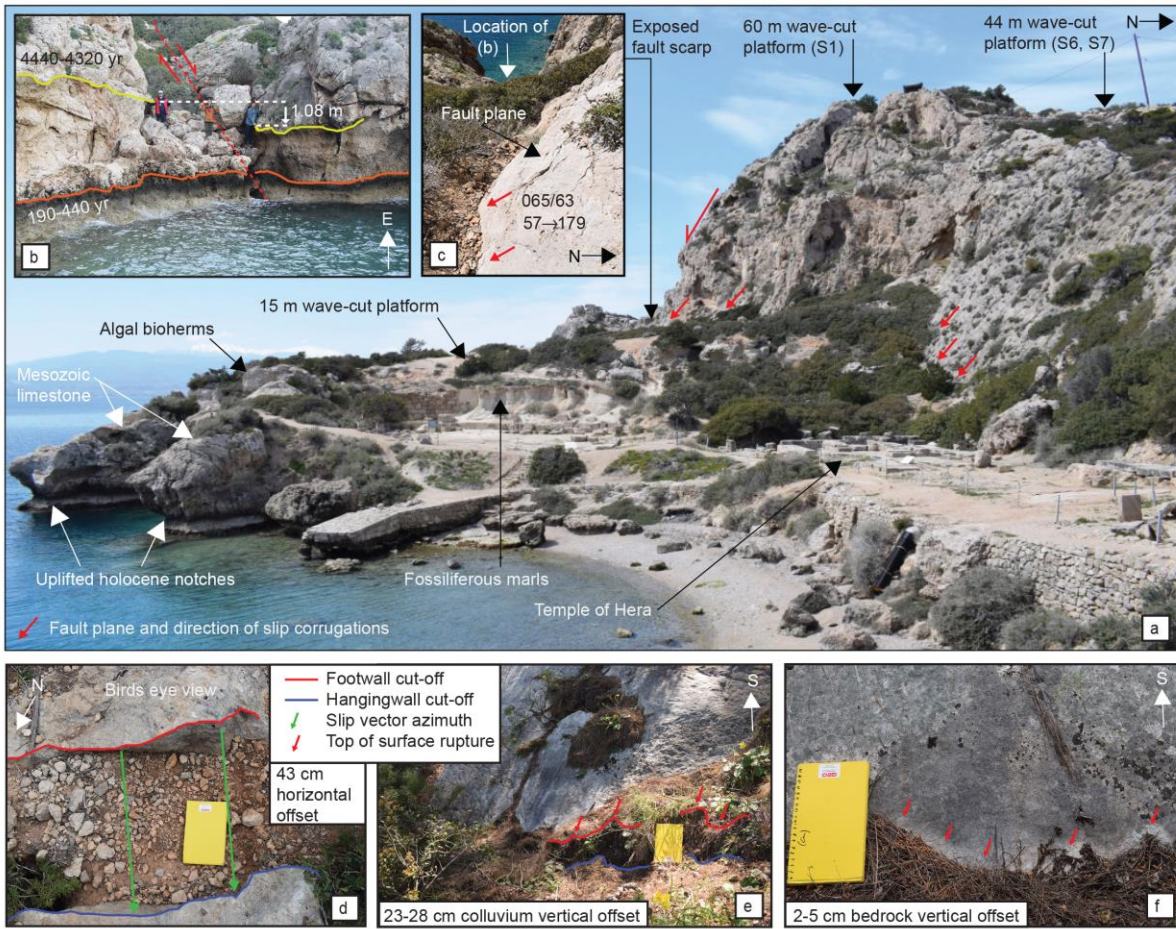
Figure 7: (a) View of Fault 1 offsetting a wave-cut platform at 60 m and 15 m. (b) Annotated photograph of offset wave-cut notches on Fault 1. (c) Fault plane and annotated direction of fault slip for Fault 1. (d) North-south horizontal offset of 43 cm on a bioherm on the north side of Cape Heraion at Locality I, Figure 4. Offset colluvium (e) and bedrock (f) along fault 17 between localities J and K, Figure 4, UTM location: 663350/4210630.
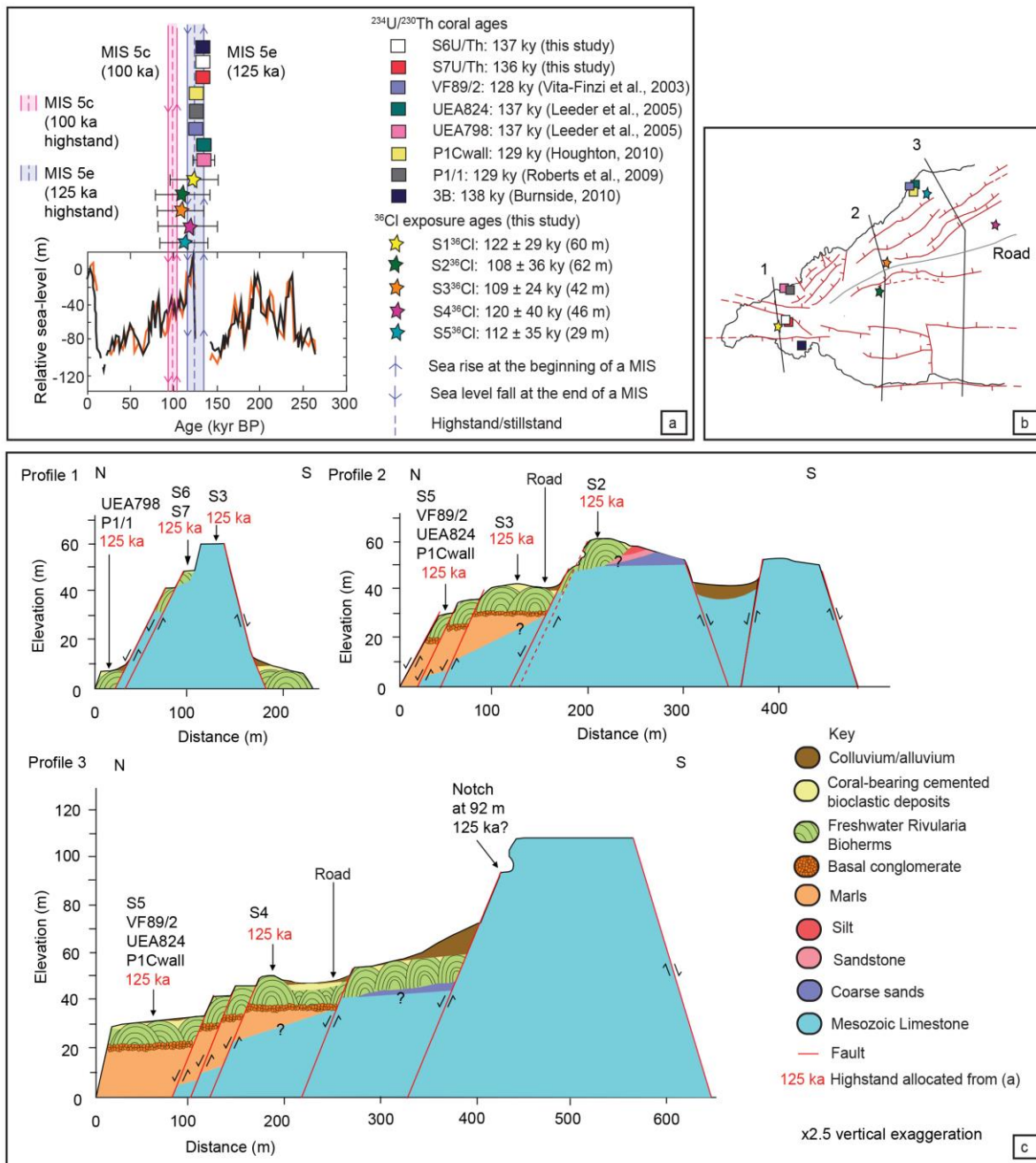
1201

Figure 8: (a) [36]Cl exposure ages and [234]U/[230]Th coral ages (where error bars are not visible, the value of error is smaller than the plot marker). Ages are plotted against the sea level curve from Siddall et al., 2003, orange and black lines represent different cores used to construct the sea-level curve. (b) Fault map and the location of profile lines from Figures 4a, b that are shown as schematic cross sections in (c).
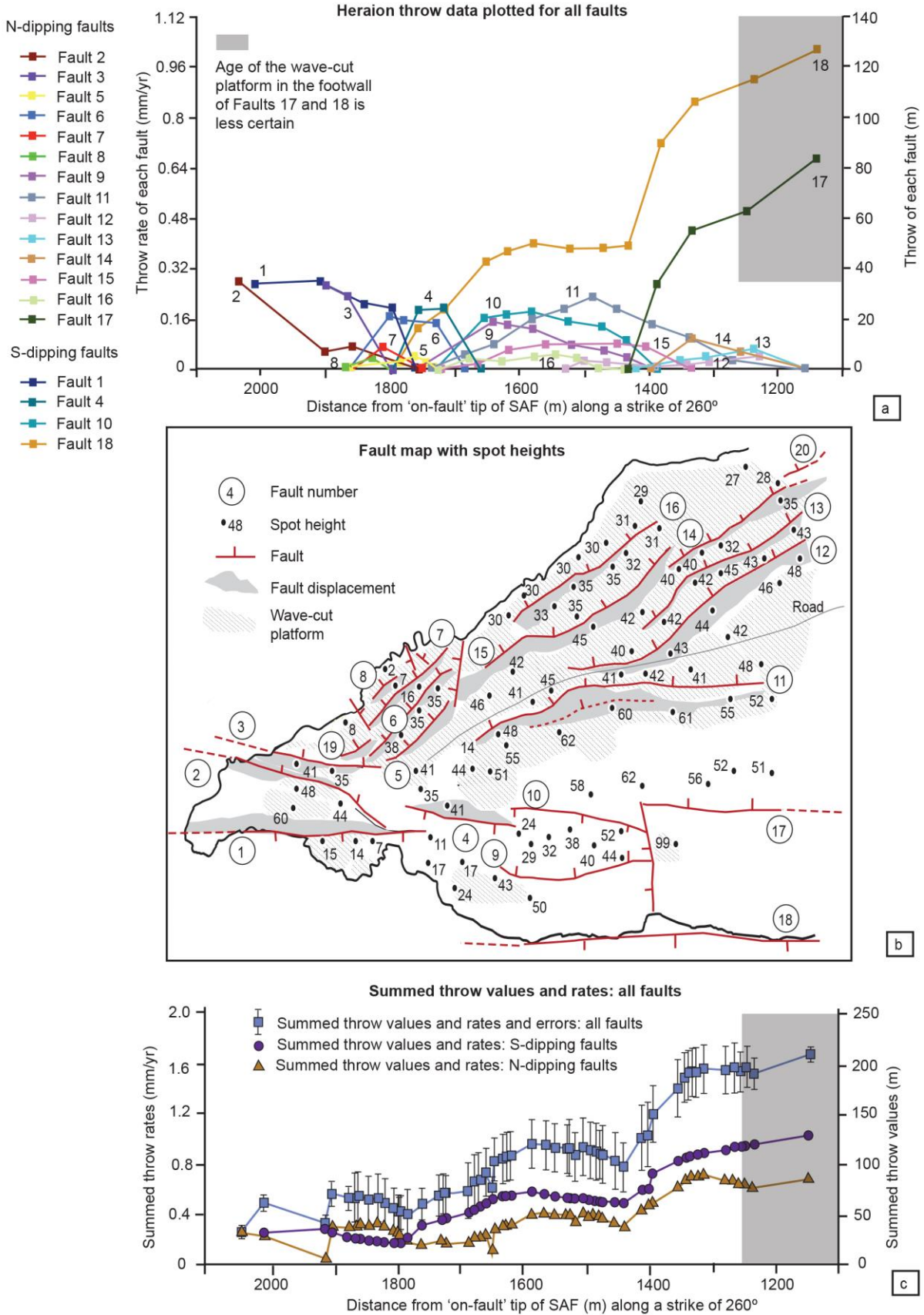
1207

Figure 9: (a) Throw profiles for individual faults constructed using elevation data (shown in
(b)). Throw values for Fault 19 is not plotted owing to a lack of elevation data. (c) Summed

1210   throw values and rates for all faults with uncertainties, summed throw values for north- and
1211   south-dipping faults. For (a) and (c) throw for each fault is plotted against the distance from
1212   the 'on-fault' tip (A) shown in Figure 2c from Morewood and Roberts (1999).
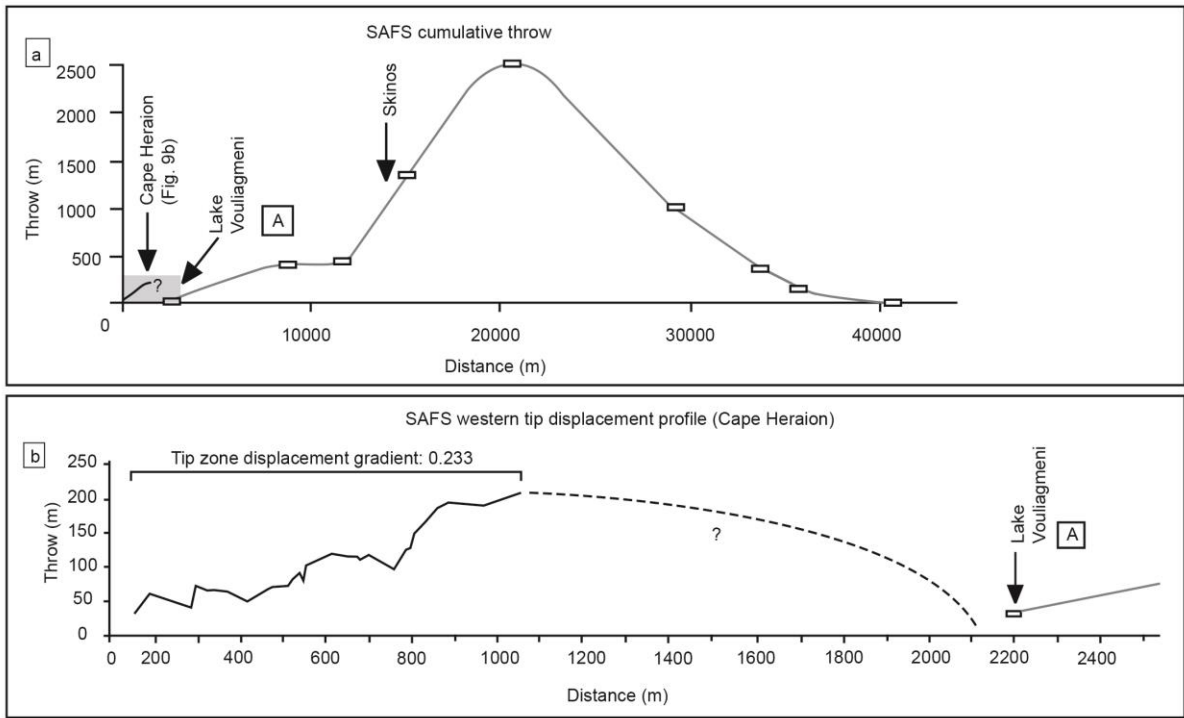
1213

1214   Figure 10: (a) Summed throw of Cape Heraion faults plotted alongside cumulative throw of
1215   the SAFS (modified from Morewood and Roberts (1999)). (b) Tip zone throw and
1216   displacement gradient from Cape Heraion. See Figure 2c for the location of A ('on-fault' tip
1217   of the SAFS).
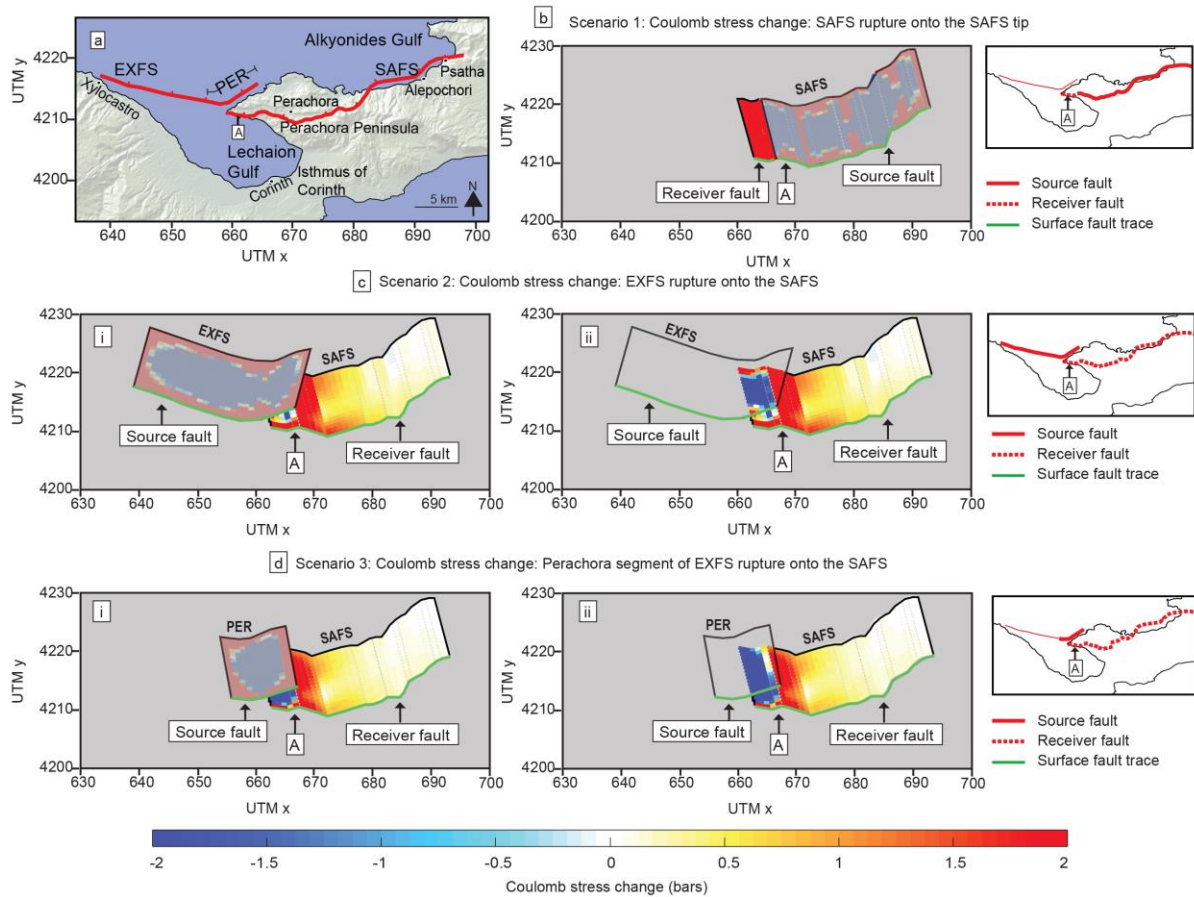
1218

1219   Figure 11: (a) Map of eastern Gulf of Corinth showing the fault traces modelled in Coulomb
1220   stress change (b-d) for the South Alkyonides Fault System (SAFS) and East Xylocastro Fault
1221   System (EXFS) (adapted from Figure 2a). See table 4 for inputs into Coulomb modelling. (b)
1222   Coulomb stress change from rupturing the source fault (entire SAFS with the exception of
1223   the western 5 km) onto the receiver fault (western 5 km section of the SAFS). (c) Coulomb
1224   stress change from rupturing the source fault (entire EXFS) onto the receiver fault (SAFS), (i)
1225   shows the source fault rupture, (ii) shows the source fault outline only. (d) Coulomb stress
1226   change from rupturing the source fault (Perachora segment of the EXFS) onto the receiver
1227   fault (SAFS), (i) shows the source fault rupture, (ii) shows the source fault outline only.

Fault number	d/L ratio
4	0.27
5	0.04
6	0.10
7	0.06
8	0.08
9	0.05
10	0.08
11	0.04
12	0.01
13	0.02
14	0.06
15	0.03
16	0.03

1228

1229   Table 1: displacement length (d/L) ratios for mapped faults on Cape Heraion, with the
1230   exception of Fault 19 due to a lack of elevation data and Faults 1, 2, 3, 17, 18, 20 as both tips
1231   could not be mapped.

Sample name	Lab ID	UTM Easting	UTM Northing	Sampling elevation (m)	Age (ky)	±2s (abs) (ky)	U (ppm)	^{232}Th (ppb)	(^{230}Th/ ^{232}Th)	(^{232}Th/ ^{238}U)	±2s (%)	(^{230}Th/ ^{238}U)	±2s (%)	(^{234}U/ ^{238}U)	±2s (%)	δ234U	±2s (%)
S6U/Th (1)	138-34	662540	4210594	44	133.5	0.7	2.42	0.005	1210.7	0.00068	0.04	0.81787	0.25	1.1354	0.14	197	±2
S6U/Th (2)	141-29	662540	4210594	44	135.4	1.2	2.44	0.006	1073.3	0.00076	0.12	0.82081	0.35	1.1315	0.28	193	±4
S6U/Th (3)	141-30	662540	4210594	44	142.7	1.3	2.57	0.006	1074.0	0.00079	0.10	0.85306	0.34	1.1429	0.25	214	±4
S6U/Th (4)	145-12	662540	4210594	44	173.7	2.0	2.13	0.009	674.9	0.00136	0.17	0.92101	0.34	1.1287	0.29	210	±5
S7U/Th (1)	138-35	662540	4210594	44	140.8	0.8	2.26	0.008	736.1	0.00114	0.04	0.83619	0.22	1.1298	0.13	193	±2
S7U/Th (2)	145-13	662540	4210594	44	139.1	0.9	2.28	0.012	467.2	0.00179	0.08	0.83630	0.25	1.1359	0.18	201	±3
S7U/Th (3)	145-14	662540	4210594	44	135.2	1.0	2.24	0.009	599.5	0.00137	0.10	0.81931	0.29	1.1301	0.21	191	±3
S7U/Th (4)	145-15	662540	4210594	44	134.5	1.0	2.34	0.014	426.6	0.00192	0.11	0.81943	0.29	1.1328	0.22	194	±3
S7U/Th (5)	145-16	662540	4210594	44	134.7	0.9	2.13	0.008	658.4	0.00125	0.09	0.82413	0.26	1.1380	0.19	202	±3
S7U/Th (6)	145-17	662540	4210594	44	132.3	0.9	2.39	0.016	364.2	0.00223	0.08	0.81141	0.29	1.1315	0.21	191	±3

1232

1233 Table 2: 234U/230Th coral age dating analytical results for samples S6U/Th and S7U/Th (see Figure 4a for sample location). Activity ratios
1234 calculated using the 234U and 230Th decay constants of Cheng et al. 2013. Activity ratios corrected for 230Th, 234U and 238U contribution
1235 from the synthetic 236U-229Th tracer, instrument baselines, mass bias, hydride formation and tailing. 230Th blanks amounting to 0.15 ± 0.03
1236 fg were subtracted from each sample. 238U blanks were on the order of 10 pg, and were negligible relative to sample size. Age and δ234U
1237 data were corrected for the presence of initial 230Th assuming an initial isotope composition of (232Th/238U) = 1.2 ± 0.6, (230Th/238U) = 1 ±
1238 0.5 and (234U/238U) = 1 ± 0.5 (all uncertainties quoted at the 2σ level).

1239

Sample name	Lithology and geomorphology	Latitude	Longitude	Elevation	Lithology	Erosion rate (mm/ky)	Total erosion (cm)	Cl (ppm)	±	^{36}Cl (atoms/g)	±	CaO (wt%)	±	Age (kyr)	Internal uncertainty (kyr)	External uncertainty (kyr)
1	Limestone: flat WCP with lithophagid borings. Sample removed from the the area displaying lithophagid borings (Fig. 6b)	38.0288	22.85106	60	Limestone	0.1	1.2	17.0503	0.2856	2327699	63421	57.41	1.38	122	3.7	29
2	Bioherm top, bioclastic sands infill spaces between adjacent bioherms. Sample removed from the top iof the bioherm (Fig. 6e)	38.0292	22.85297	62	Bioherm	6	64.8	22.5328	0.4739	1195064	34923	43.85	1.53	108	8.4	36
3	Bioclastic packstone, excellent millholes preserved. Ssample removed from immediately adjacent to the millhole (Fig. 6f)	38.0304	22.85522	42	Packstone	0.1	1.1	38.7794	0.8003	1887336	54970	49.02	1.52	109	3.5	24
4	Bioherm top, millholes, abundant lithophagid borings preserved on the adjacent backwall (Fig. 6g)	38.032	22.8596	46	Bioherm	6	72.0	33.3263	0.6646	1616569	47009	53.80	1.47	120	8.8	40
5	Bioherm top, visible above surrounding alluvium (Fig. 6h)	38.0305	22.85516	29	Bioherm	6	67.2	60.5561	1.6227	1684932	46140	54.01	1.44	112	9.3	35

1240

1241

1242   Table 3: ^{36}Cl exposure dating analytical results and sample descriptions (see Figure 4a for the sample location). ^{36}Cl concentrations are based

1243   on 1.2x10^{-12} ^{36}Cl/Cl ratio for Z93-0005 (PRIME Lab, Purdue). This standard agrees with standards prepared by K. Nishiizumi, which were used as

1244   secondary standards. Cl concentrations were determined by AMS isotope dilution (Stuart and Dunai, 2009). ^{36}Cl/Cl processed blank ratios

1245   ranged between 2.4 and 6.03% of the samples ^{36}Cl/Cl ratios.

Fault name	Fault information (fault trace, kinematics)	Length (km)	Depth of seismogenic zone (km)	Dip °	Facing direction °	Rake °	Sub-surface maximum slip value (m)	Max. Mw	Figure
East Xylocastro Faut System (EAFS)	Whole fault length is used combining fault traces of the East Xylocastro Fault, North Kiato Fault and Perachora Fault as per Nixon et al., 2016.	29	15	55	010	-90	1.6	6.53	11b
Perachora Fault (EXFS)	Fault trace from Nixon et al., 2016	11	15	55	350	-90	1.4	6.21	11c
South Alkyonnides Fault System (SAFS)	Whole fault length is used as per Roberts et al., 2009 (rupturing the Pisia, East Alkyonides and Psatha faults), with the exception of western 5 km tip zone. Dip data averaged from Jackson et al., 1982 (45°) and Mechernich et al., 2016 (60°)	38.7	15	55	345	-90	2.4	6.74	11a

1246

1247   Table 4: Inputs for Coulomb stress change modelling. Slip at the surface is set at 0.1 (10%) of the slip value at depth. This value is based upon

1248   the relationship between surface slip (Vittori et al., 2011) and maximum slip values at depth (Wilkinson et al., 2015) for the Mw 6.3 2009

1249   L'Aquila Earthquake, Italy

1250   Supplementary 1:

1251   Description of the observed stratigraphy on Cape Heraion to accompany Figures 4a and 5)

1252

1253   At the base of the stratigraphic column is Mesozoic limestone (Figures 4a, 5, Locality A).

1254   Unconformably above the limestone is a sedimentary succession, only observed in the centre

1255   of the cape, that fines up from coarse sands to silts (Locality D, Figure 4a and Figure 5). Plio-

1256   Pleistocene marls are inferred to occur stratigraphically above the sands and silts although

1257   the contact between them has not been observed, and they may be lateral equivalents. The

1258   marls form large cliff outcrops along the north of the cape (e.g. Locality F in Figures 4 and 5)

1259   and are overlain by a coarse boulder conglomerate that displays an erosive base cut into the

1260   underlying marls (Locality F). Algal carbonate bioherms formed of *Rivularia haematities* have

1261   grown on the basal conglomerate (Localities E, F and G, Figure 5) and directly on the basement

1262   limestone (Localities B, C and D, Figure 5). In turn, the bioherms are overlain by fossiliferous,

1263   coral-bearing, marine bioclastic sands preserved as a continuous 0.6-1.0 m thick layer

1264   (Localities B, C, E, F and H, Figures 4a, 5) or as patches infilling cavities between or within the

1265   bioherms (Locality C and D Figure 4a, 5). These bioclastic deposits have rich fossil assemblages

1266   with colonies of the branching coral *Cladocora caespitosa* in life position, frameworks of

1267   serpulid worm tubes, and bivalves, pecten, turritella, bryozoa, and elsewhere broken

1268   fragments of *Cladocora caespitosa* within the sediment that form death assemblages. In

1269   places, the inside of the bioherms has been eroded and small caves have formed, which have

1270   been bored by lithophagids (Figure 5). The caves contain marine deposits such as *Cladocora*

1271   *caespitosa* (e.g. Locality C), suggesting the cave-filling deposits are the age-equivalents of the

1272   coral-bearing bioclastic sands that lie on top of the bioherms.

Supplementary 2

1: Sample Name	2: Scaling (Select One)	3: Latitude decimal degrees	4: Longitude decimal degrees	5: Elevation meters	6: Pressure hPa	7: Atmospheric Pressure or Elevation	8: Sample Thickness cm	9: Bulk Density g/cm 3	10: Shielding Factor unitless	11: Erosion Rate mm/kyr	12: Conc. 36Cl Atoms of 36 Cl/g of sample	13: Attenuation length g/cm 2	14: Depth to Top of Sample g/cm 2	15: Year Collected Year A.D.	16: Water Content in Pores volume fraction	17: Mineral Separation (Select One)	18: Bulk Rock SiO2 oxide weight %	19: Bulk Rock TiO2 oxide weight %	20: Bulk Rock Al2O3 oxide weight %
1	DE	38.02877	22.851055	60		Elevation	3.7	2.649	0.9999	0.1	2327699	160	0	2000	0.01	No	0	0	0
2	DE	38.02919	22.852974	62		Elevation	4	2.565	0.9999	6	1195064	160	0	2000	0.01	No	0	0	0
3	DE	38.03036	22.855224	42		Elevation	3.4	2.565	0.9981	0.1	1887336	160	0	2000	0.01	No	0	0	0
4	DE	38.03203	22.859599	46		Elevation	4.5	2.233	0.9999	6	1616569	160	0	2000	0.01	No	0	0	0
5	DE	38.03046	22.855155	29		Elevation	4.1	2.565	0.9995	6	1684932	160	0	2000	0.01	No	0	0	0

| 21: Bulk Rock Fe2O3 oxide weight %	22: Bulk Rock MnO oxide weight %	23: Bulk Rock MgO oxide weight %	24: Bulk Rock CaO oxide weight %	25: Bulk Rock Na2O oxide weight %	26: Bulk Rock K2O oxide weight %	27: Bulk Rock P2O5 oxide weight %	28: Analytical Water weight %	29: Bulk Rock CO2 oxide weight %	30: Bulk Rock Cl ppm	31: Bulk Rock B ppm	32: Bulk Rock Sm ppm	33: Bulk Rock Gd ppm	34: Bulk Rock U ppm	35: Bulk Rock Th ppm	36: Bulk Rock Cr ppm	37: Bulk Rock Li ppm	38: Target K2O weight %	39: Target CaO weight %	40: Target TiO2 weight %
0.05148	0	0.00	57.38099	0	0.00000	0	1.00000	42.56753	17.05027	0	0	0	0	0	0	0	0.00000	57.41238	0.00000
0.02843	0	0.00	43.82164	0	0.00000	0	1.00000	56.14993	22.5328	0	0	0	0	0	0	0	0.00000	43.84561	0.00000
0.061312	0	0.00	48.98905	0	0.00000	0	1.00000	50.94964	38.77938	0	0	0	0	0	0	0	0.00000	49.01585	0.00000
0.02793	0	0.00	53.77027	0	0.00000	0	1.00000	46.20180	33.32635	0	0	0	0	0	0	0	0.00000	53.79968	0.00000
0.120106	0	0.00	53.98398	0	0.00000	0	1.00000	45.89592	60.55609	0	0	0	0	0	0	0	0.00000	54.01351	0.00000

41: Target Fe2O3 weight %	42: Target Cl ppm	43: Latitude Uncertainty decimal degrees	44: Longitude Uncertainty decimal degrees	45: Elevation Uncertainty meters	46: Pressure Uncertainty hPa	47: Sample Thickness Uncertainty cm	48: Bulk Density Uncertainty g/cm 3	49: Shielding Factor Uncertainty unitless	50: Erosion-Rate Uncertainty mm/kyr	51: Conc. 36 Cl Uncertainty Atoms of 36 Cl/g of sample	52: Attenuation Length Uncertainty g/cm 2	53: Depth to Top of Sample Uncertainty g/cm 2	54: Year Collected Uncertainty Year A.D.	55: Water Content in Pores Uncertainty Volume %	56: Bulk Rock SiO 2 Uncertainty oxide weight %	57: Bulk Rock TiO 2 Uncertainty oxide weight %	58: Bulk Rock Al 2 O 3 Uncertainty oxide weight %	59: Bulk Rock Fe 2 O 3 Uncertainty oxide weight %	60: Bulk Rock MnO Uncertainty oxide weight %
0.05148	17.05	0	0	10		0.5	0.2	0	0	63421	10	0	10	0.01	0	0.0000	0	0.46670195	0
0.02843	22.53	0	0	10		0.5	0.2	0	0	34923	10	0	10	0.01	0	0.0000	0	0.51572725	0
0.061312	38.78	0	0	10		0.5	0.2	0	0	54970	10	0	10	0.01	0	0.0000	0	0.51356044	0
0.02793	33.33	0	0	10		0.5	0.2	0	0	47009	10	0	10	0.01	0	0.0000	0	0.49714071	0
0.120106	60.56	0	0	10		0.5	0.2	0	0	46140	10	0	10	0.01	0	0.0000	0	0.48551267	0

1273

1274

1275

1276

61: Bulk Rock MgO Uncertainty oxide weight %	62: Bulk Rock CaO Uncertainty oxide weight %	63: Bulk Rock Na 2 O Uncertainty oxide weight %	64: Bulk Rock K 2 O Uncertainty oxide weight %	65: Bulk Rock P 2 O 5 Uncertainty oxide weight %	66: Analytical Water Uncertainty weight %	67: Bulk Rock CO 2 Uncertainty oxide weight %	68: Bulk Rock Cl Uncertainty ppm	69: Bulk Rock B Uncertainty ppm	70: Bulk Rock Sm Uncertainty ppm	71: Bulk Rock Gd Uncertainty ppm	72: Bulk Rock U Uncertainty ppm	73: Bulk Rock Th Uncertainty ppm	74: Bulk Rock Cr Uncertainty ppm	75: Bulk Rock Li Uncertainty ppm	76: Target K2O Uncertainty weight %	77: Target CaO Uncertainty weight %	78: Target TiO2 Uncertainty weight %	79: Target Fe2O3 Uncertainty weight %	80: Target Cl Uncertainty ppm	81: Covariance unitless
0	1.3804232	0	0.0000	0	1.00000	1.3804232	0.28561763	0	0	0	0	0	0	0	0.00000	1.3804232	0.00000	0.46670195	0.28561763	0
0	1.5254315	0	0.0000	0	1.00000	1.5254315	0.47391526	0	0	0	0	0	0	0	0.00000	1.5254315	0.00000	0.51572725	0.47391526	0
0	1.51902247	0	0.0000	0	1.00000	1.51902247	0.80026479	0	0	0	0	0	0	0	0.00000	1.51902247	0.00000	0.51356044	0.80026479	0
0	1.47045576	0	0.0000	0	1.00000	1.47045576	0.66456149	0	0	0	0	0	0	0	0.00000	1.47045576	0.00000	0.49714071	0.66456149	0
0	1.43606203	0	0.0000	0	1.00000	1.43606203	1.62273089	0	0	0	0	0	0	0	0.00000	1.43606203	0.00000	0.48551267	1.62273089	0

1277

1278   Supplement 2: Input data for CRONUScalc to determine ages of ^{36}Cl exposure samples

1279   Supplementary 3
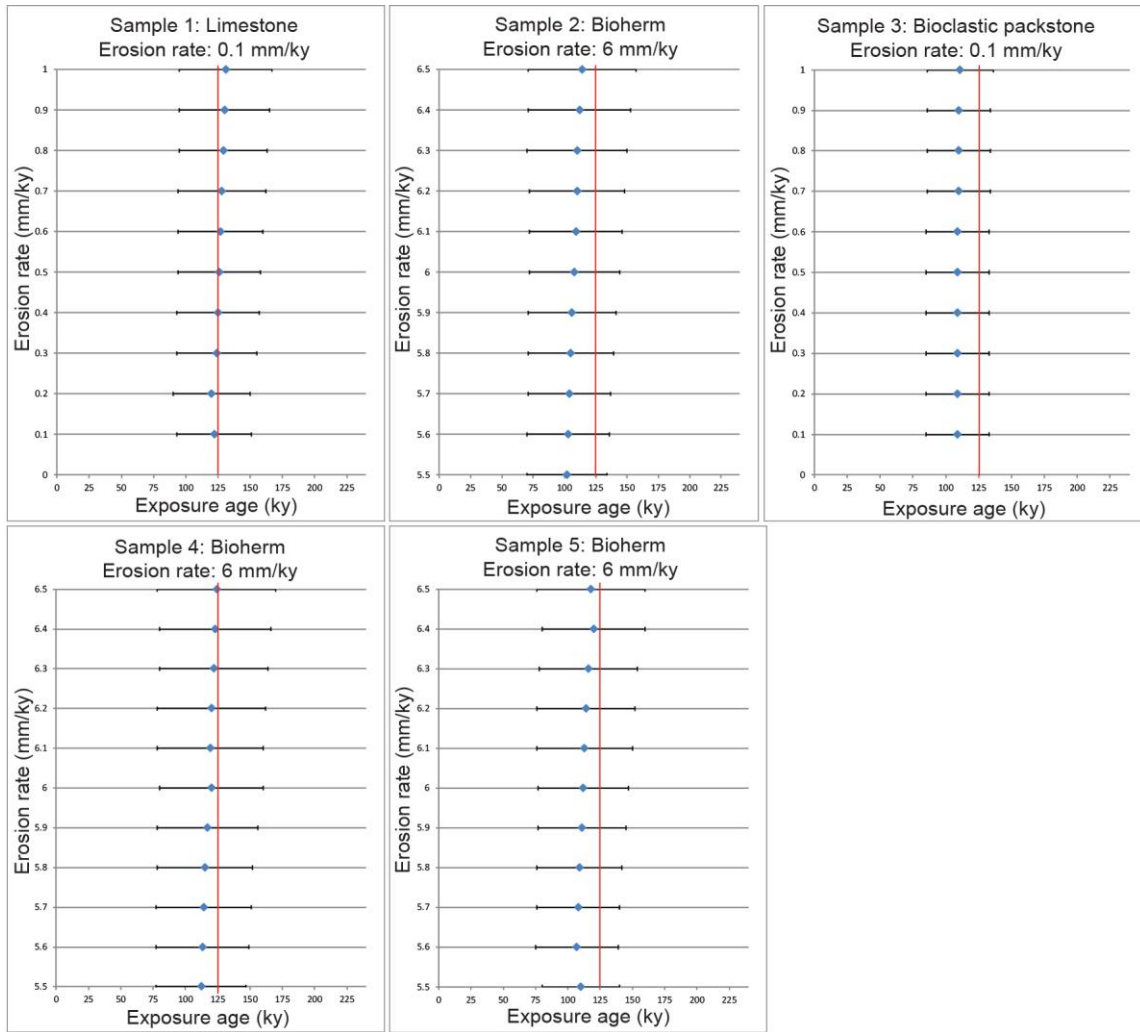
1280

1281   Supplement 3: Sensitivity tests for the erosion rates of 0.1-1.0 mm/ky for samples 1 and 3, and of
1282   5.5-6.5 mm/yr for samples 2, 4 and 5.

1283